ARTICLE IN PRESS

Ceramics International xxx (xxxx) xxx

Contents lists available at ScienceDirect

Ceramics International

journal homepage: www.elsevier.com/locate/ceramint

Synthesis and Biochemical/Biomechanical Characterization of Borate glass/Hydroxyapatite Composites: A Comparative Study on Weight ratios and Mixing order

Neda Sami, Sahar Mollazadeh Beidokhti *, Jalil Vahdati Khaki **

Department of Materials Engineering, Faculty of Engineering, Ferdowsi University of Mashhad (FUM), Azadi Sq., Mashhad, Iran

ARTICLE INFO

Handling Editor: Dr P. Vincenzini

Keywords:
Glass/ceramic nanocomposite
Borate glass
Hydroxyapatite
Solution combustion synthesis
Spark plasma sintering

ABSTRACT

An engineered tissue with bioactivity and proper mechanical properties could address the challenge of regenerating damaged tissues. Hydroxyapatite (HA), a ceramic akin to natural bone, is a potential bone substitute. However, its low mechanical strength and minimal degradability in physiological environments limit its effectiveness. This study aims to develop a composite with enhanced mechanical properties and bioactivity for bone regeneration. Accordingly, HA was combined with 13–93B3 borate bioactive glass (BG) to form composite powders using solution combustion synthesis (SCS) via two methods, which varied in BG:HA ratios and mixing order. In these methods, pre-prepared particles of one phase are added to the solution of the other phase. The mixture is then placed in the synthesis chamber. A spark plasma sintering procedure produced a tablet form of the composites. For comparison, a control tablet with separate BG and HA particles was also prepared. The interface's connections in control composite were modeled using Material Studio. The final samples were analyzed for physical, mechanical, and biological properties. Accordingly, the 75 % HA-containing samples were considered optimal, as they exhibited the highest crystallinity index and the lowest undesirable phase. These samples also showed a particle size range of 30–50 nm, confirming the nanoscale size observed in TEM and PSA results. Also, their FESEM images confirmed the presence of both BG and HA phases. Additionally, the variation in microhardness values, ranging from 68 to 151 Vickers, reflects differences in synthesis methods. Bioactivity was also assessed by immersing samples in simulated body fluid (SBF) over time. After 28 days of immersion, more intense HA peaks, a reduction in Ca^{2+} and PO_4^{3-} concentrations, and the presence of a P-O band around 1830 cm^{-1} indicated the formation of the bone phase. Furthermore, it was confirmed that the mechanical properties can be maintained even after immersion in SBF.

1. Introduction

One of the most captivating fields of study in materials science is the advancement of bioceramics for bone reconstruction surgery, which seeks to repair damaged tissues from injuries [1]. Key considerations include biocompatibility, biodegradability, mechanical properties, and alignment with target tissue structure. Therefore, the development of advanced bioceramics that promote healing in biological tissues is crucial for addressing bone defects in regenerative medicine [2–4]. Accordingly, hydroxyapatite (HA) is the most commonly used bioceramic in orthopedic applications based on its similarity to the mineral composition of human bone. It is favored for its biocompatibility and osteoconductivity [5]. It is used in powdered or granular forms in various oral, maxillofacial, and orthopedic applications [6]. Additionally, it is employed to create bioactive coatings on metal implants. These coatings enhance the oleophilic properties of the implants, which in turn improves the bonding between bone and the implant [7,8].

However, hydroxyapatite suffers from low mechanical strength and exhibit minimal degradability in a physiological environment, meaning they cannot be resorbed or replaced by newly formed bone [9,10]. This results in inadequate osteoinductivity for tissue regeneration at the required rate [11]. A potential solution to address HA's issues is to enhance HA by incorporating a bioactive glassy phase to create a composite. Bioactive glasses exhibit a greater bioactivity index in

* Corresponding author.
** Corresponding author.
E-mail addresses: Mollzadeh.b@um.ac.ir (S.M. Beidokhti), vahdati@um.ac.ir (J.V. Khaki).

https://doi.org/10.1016/j.ceramint.2025.09.405
Received 25 May 2025; Received in revised form 5 September 2025; Accepted 25 September 2025
Available online 25 September 2025

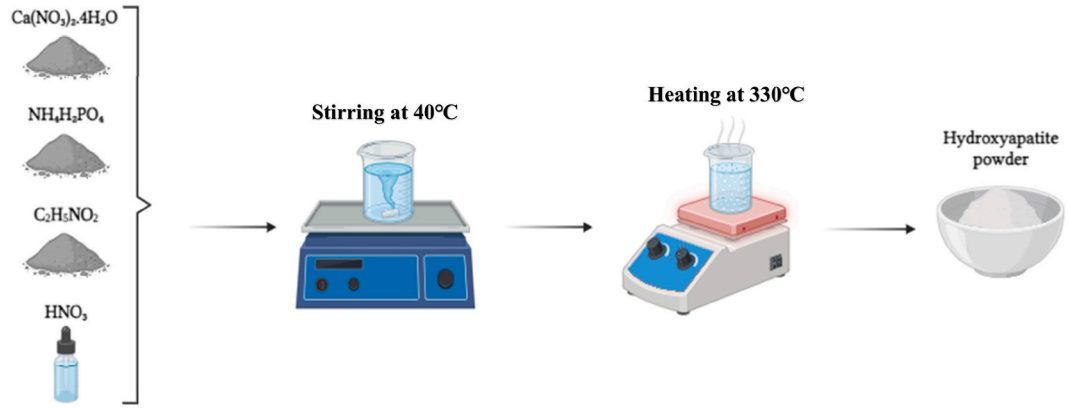

Fig. 1. Schematic of the steps for the synthesis of hydroxyapatite nanopowder.

comparison to HA. Researches had shown that glass-reinforced hydroxyapatite (HA) demonstrates improved bioactivity compared to standard commercial HA. Lately, there has been a growing interest in borate glasses specially 13–93B3, due to the promising medical outcomes related to healing [12–14]. Recent studies suggest that boron deficiency reduces bone volume and trabecular thickness, leading to malignant bone irregularities. Boron supplementation may enhance wound healing, growth factor release, RNA synthesis, and extracellular matrix turnover [15,16]. Also, the response of the tissue might be attributed to their rapid dissolution, which occurs at a faster rate than that of silica-based glasses specially 45S5 that was primalrily discovered by L.Hench [17,18]. Recently, Ghanad et al. [13] and Akrami et al. [14] demonstrated that a simple and cost-effective solution combustion synthesis (SCS) can create highly porous 1393-B3 borate-based glasses. Therefore, incorporating appropriate quantities of BG also aids in the solidification of HA powders, allowing for reduced temperature requirements to produce bulk products that has been reported by various researchers [19–21]. Besides, the high temperatures (1200–1350 °C) used for traditional sintering of HA/BG composites can cause complete crystallization of BG and excessive interactions with HA, which may reduce bioactivity [22]. Additionally, crystallization adversely affects the sintering process, impacting HA densification. This issue could be addressed by using non-traditional sintering methods to reduce heat exposure and minimize crystallization [23]. A novel technique is the spark plasma sintering (SPS) method, where high-energy electric sparks purify and activate particles more rapidly than conventional sintering, resulting in quick and higher densification [24]. The SPS method quickly densifies ceramics at lower temperatures, saving energy and costs while preserving fine grain structures and enhancing mechanical properties [25]. In a research by Bellucci et al. [23], HA/BG(a silica-based glass) composites were fabricated through the SPS method in ratios of 50:50, 80:20, and 30:70. It was observed that maintaining a temperature of 770 °C for 10 min with an 80:20 ratio yielded effective composites suitable for bone tissue repair, exhibiting high density and favorable bioactivity.

In this study, spark plasma sintering method was utilized to convert the final HA/BG (in different weight ratios) composite powders into tablets. The initial composite powders were synthesized via a solution combustion method (SCS). The mentioned SCS method is proposed for the synthesis of a pre-synthesis solution of one phase (HA or BG) in the presence of pre-prepared particles of the other phase (BG or HA), resulting in composite powders that consist of both HA and BG phases. Moreover, the final set and production material combines borate glass and hydroxyapatite ceramic to affect the release rate of ions in the body's environment and the final mechanical properties [21,26]. Based on the a research [13], 13–93B3 borate glass begins to devitrify at temperatures above 700 °C. Therefore, SPS was conducted at 700 °C to prevent devitrification and minimize reactions between HA and BG. Also, a longer holding times was utilized to ensure sufficient sintering and mass transport, facilitating ionic substitution in HA, which is essential for stabilizing the HA phase and preventing devitrification of the glass [23,27]. To study how the mixing orders in the composite powders affects their bulk properties, a control tablet made of separate HA and BG powders was fabricated via SPS. Furthermore, the present study investigates the potential of composite formation at the interface of BG and HA separate powders in control tablet via dynamic simulation. It aims to understand the feasibility of combining these two materials into a uniform composite by analyzing the interactions at the atomic level. The simulations offer insights into the conditions and mechanisms that promote the formation of a composite structure, highlighting their potential applications across various industrial fields. In addition, the synthesized samples were conducted through investigations, including X-ray diffraction analysis (XRD), Field emission scanning electron microscopy (FESEM), Transmission Electron Microscopy (TEM), Dynamic Light Scattering Particle Size Distribution Analysis (DLS/PSA), Inductively Coupled Plasma Optical Emission Spectroscopy (ICP-OES), and microhardness analysis. Mechanical analyses and so on were utilized. Notably, this research is distinct in that it produced in situ 13–93B3 bioactive glass-ceramic composite samples, a deviation from previous methodologies that relied on pre-prepared powders. This novel approach holds the potential for significant tissue repair and bioengineering advancements.

2. Materials and method

2.1. Preparation of hydroxyapatite powder

For the preparation of hydroxyapatite particles ($Ca_5(PO_4)_3OH$), there were several chemicals, including calcium nitrate tetrahydrate ($Ca(NO_3)_2.4H_2O$, 99.95 %, Merck), ammonium dihydrogen phosphate ($NH_4H_2PO_4$, 99.99 %, Merck). Also, glycine ($C_2H_5NO_2$, Merck) was used as fuel. Additionally, nitric acid (HNO_3, 65 %, Dr. Mojallali) as a fuel-aid and deionized water were used as a solvent in the synthesis process. All chemicals used were of analytical grade without the requirement for further purification for the solution combustion synthesis (SCS) process. The fuel-to-oxidizer ratio was φ = 1.00 for the synthesizing of hydroxyapatite nanoparticles based on the mentioned equation as Eq (1):

$$\rightarrow 45\,Ca(NO_3)_2.4H_2O + 27\,NH_4H_2PO_4 + 41\,C_2H_5NO_2 = 9\,Ca_5(PO_4)_3OH + 82\,CO_2 + 359\,H_2O + 79\,N_2 \quad \text{Eq (1)}$$

In this case (as shown in Fig. 1), the precursors were dismounted of deionized water and mixed well using a magnetic stirrer. The final solution was then heated to initiate a combustion synthesis reaction to produce final nanopowders.

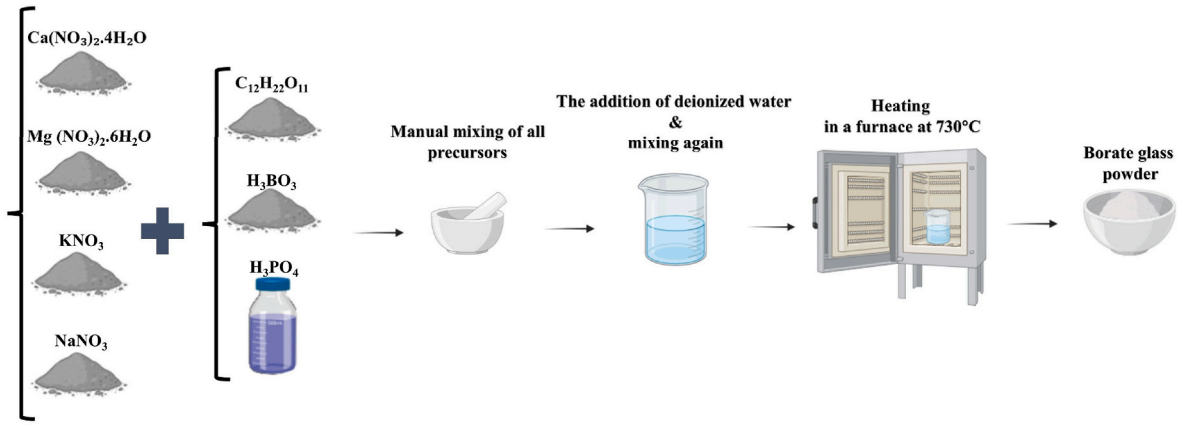

Fig. 2. Schematic of the synthesis steps of borate glass nanopowder.

Table 1
Coding system of the synthesized samples in the present study.

Powders (P)					
HA: BG (wt%)	Hydroxyapatite (HA)	Borate bioactive glass (BG)	BG powder + HA solution (I)	HA powder + BG solution (II)	HA powder + BG powder
100:0	100 %HA-P	–	–	–	–
80:20	–	100 %BG-P	80 %HA-I-P	80 %HA-II-P	80 %HA-III-P
75:25	–	–	75 %HA-I-P	75 %HA-II-P	75 %HA-III-P
50:50	–	–	50 %HA-I-P	50 %HA-II-P	50 %HA-III-P
25:75	–	–	25 %HA-I-P	25 %HA-II-P	25 %HA-III-P
20:80	–	–	20 %HA-I-P	20 %HA-II-P	20 %HA-III-P
0:100	–	–	–	–	–
Tablets (T)					
HA: BG (wt %)	Hydroxyapatite (HA)	Borate bioactive glass (BG)	BG powder + HA solution (I)	HA powder + BG solution (II)	HA powder + BG powder
100:0	–	–	–	–	–
80:20	–	–	80 %HA-I-T	80 %HA-II-T	80 %HA-III-T
75:25	–	–	75 %HA-I-T	75 %HA-II-T	75 %HA-III-T
50:50	–	–	50 %HA-I-T	50 %HA-II-T	50 %HA-III-T
25:75	–	–	25 %HA-I-T	25 %HA-II-T	25 %HA-III-T
20:80	–	–	20 %HA-I-T	20 %HA-II-T	20 %HA-III-T
0:100	–	–	–	–	–

2.2. Preparation of 13–93B3 bioactive glass powder

There were several precursors for the preparation of borate-based 1393-B3 glass [13,14] powders (with a composition of $54.6B_2O_3$–$6Na_2O$–$7.9K_2O$–$7.7MgO$–$22.1CaO$-$1.7P_2O_5$), including calcium nitrate tetrahydrate ($Ca(NO_3)_2.4H_2O$, 99.95 %, Merck), magnesium nitrate hexahydrate ($Mg(NO_3)_2.6H_2O$), 99.00 %, Sigma-Aldrich), potassium nitrate (KNO_3, 99.00 %, Sigma-Aldrich) and sodium nitrate ($NaNO_3$, 99.00 %, Sigma- Aldrich). All the mentioned precursors were dissolved in a certain amount of deionized water. H_3BO_3 and H_3PO_4 were added to the solution and stirred to obtain a homogeneous system. Sucrose ($C_{12}H_{22}O_{11}$, Edible-grade) was then added as fuel content. The final homogeneous mixture was then heated (in a furnace at 730 °C) to undergo combustion synthesis (Fig. 2). It is believed that the reaction is complete once the final white powder is obtained [13]. The reaction equation (Eq (2)) with φ = 0.84 is as follows:

$$\begin{aligned}\rightarrow & 12\,NaNO_3 + 15.8\,KNO_3 + 22.1\,Ca(NO_3)_2.4H_2O \\ & + 7.7\,Mg(NO_3)_2.6H_2O + 109.2\,H_3BO_3 \\ & + 3.4\,H_3PO_4 + 3.856\,C_{12}H_{22}O_{11} \\ & = 0.4235\,[54.6\,B_2O_3 + 22.1\,CaO + 7.9\,K_2O \\ & + 7.7\,MgO + 6Na_2O + 1.7\,P_2O_5] + 6.917\,NaNO_3 \\ & + 9.108\,KNO_3 + 12.74\,Ca(NO_3)_2.4H_2O \\ & + 4.439\,Mg(NO_3)_2.6H_2O + 62.948\,H_3BO_3 \\ & + 1.96\,H_3PO_4 + 46.272\,CO_2 + 170.96\,H_2O + 18.5085\,N_2\end{aligned}$$

Eq (2)

2.3. Preparation of composites powder

Two primary methods were employed to produce composite powders as methods I and II. For method I, borate glass powders were synthesized using the method outlined in section 2.2). Subsequently, these powders underwent fine grinding. Following this, a solution of hydroxyapatite's precursors ready for synthesis was prepared, into which the aforementioned glass powders were incorporated and stirred immediately before ignition. This mixing process involved varying weight ratios of hydroxyapatite and borate glass, as detailed in Table 1. Notably, the conditions employed during combustion synthesis align entirely with those of pure hydroxyapatite synthesis. Method II's sequence of steps is reversed compared to method I. Primarily, hydroxyapatite powder is synthesized following the procedure outlined in section 2.1), and subjected to fine grinding. Afterward, the final solution for borate glass synthesis was prepared, and hydroxyapatite particles were added to it with specific weight ratios as indicated in Table 1. Following manual mixing, all synthesis steps are executed consistent with the pure borate glass synthesis process.

2.4. Preparation of composite tablets

The spark plasma sintering (SPS) method was used to prepare the final tablets. As mentioned earlier, it is necessary to determine the temperature, holding time, and applied pressure in SPS. Taking into account the studies conducted by other researchers [21,23,26,28,29] and determining that 75 % hydroxyapatite content is optimal based on the results discussed later, a temperature of 700 °C and a pressure of 16 MPa were chosen as the parameters for the spark plasma sintering (SPS) process with the duration of 15 min. In other words, the requirement for elevated temperature, pressure, and duration can be attributed to 75 % hydroxyapatite in the structure. However, this study did not account for

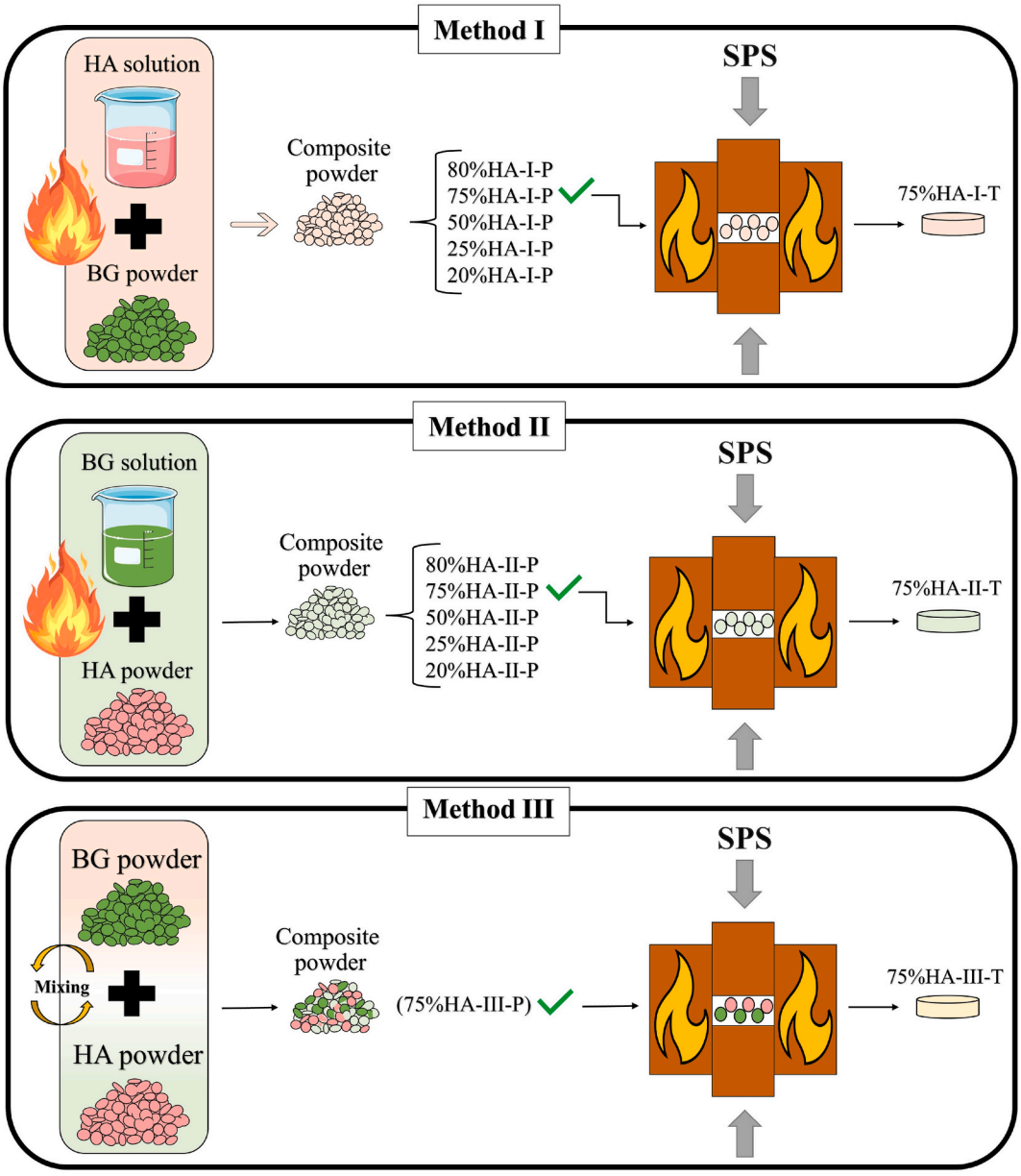

Fig. 3. Schematic of the procedure for manufacturing of the final tablets based on three different menthods.

a higher temperature increase caused by the 25 % glass content and the potential for its decomposition and destruction at temperatures above 700 °C. As a result, all the composite tablets were subjected to the same heat treatment program to prevent any unwanted glass transformation. Table 1 and Fig. 3 show all samples' coding systems and specifications. Moreover, a control tablet was also prepared based on the physical mixing (hand grinding) of pure glass and hydroxyapatite powder in the optimal ratio (method III) to enable the meaningful comparison between the samples. Also, a study on a ceramic powders system demonstrated that after 30 min of mixing, maximum uniformity was achieved. Extending the mixing time did not further improve the distribution of the mixture. It was proved that 15–30 min of manual mixing are sufficient to produce uniform blends for ceramic and glass-ceramic systems. Therefore, at least 30-min of mixing time was chosen [30]. As a result, a dry mixing method using an agate mortar was employed instead of a wet mixing method to prevent the introduction of moisture into the glassy phase. Hence, to prepare the control sample, a certain weight of both BG and HA powders was first weighed. Then these particles were pounded well with a mortar for about 10 min. Then, these two powders were added to each other and pounded again for 10 min. They were then visually inspected, and the particles adhering to the mortar were separated from it. Then they were pounded again with a mortar for another 10–15 min for more uniformity.

Furthermore, simulations were performed as follow to check the possibility of the two phases to form stable interfaces and supporting the use of simple mixing for the composite.

2.5. Simulation of composite interface via molecular dynamics

To investigate the behavior of the control composite at the interface of two powders, modeling of bonds and atoms was used with the help of the computer simulation software Material Studio. Fig. 4 shows all the steps and results of the simulation in the form of a graphical summary. The atomic arrangement of each of the two phases was primarily prepared, and the necessary investigations were carried out on them. The disordered atomic network of borate glass consists of 6 different oxides. According to formula $54.6B_2O_3$-$6Na_2O$-$7.9K_2O$-$7.7MgO$-$22.1CaO$-$1.7P_2O_5$, each of these six oxides has a specific molar content in the final

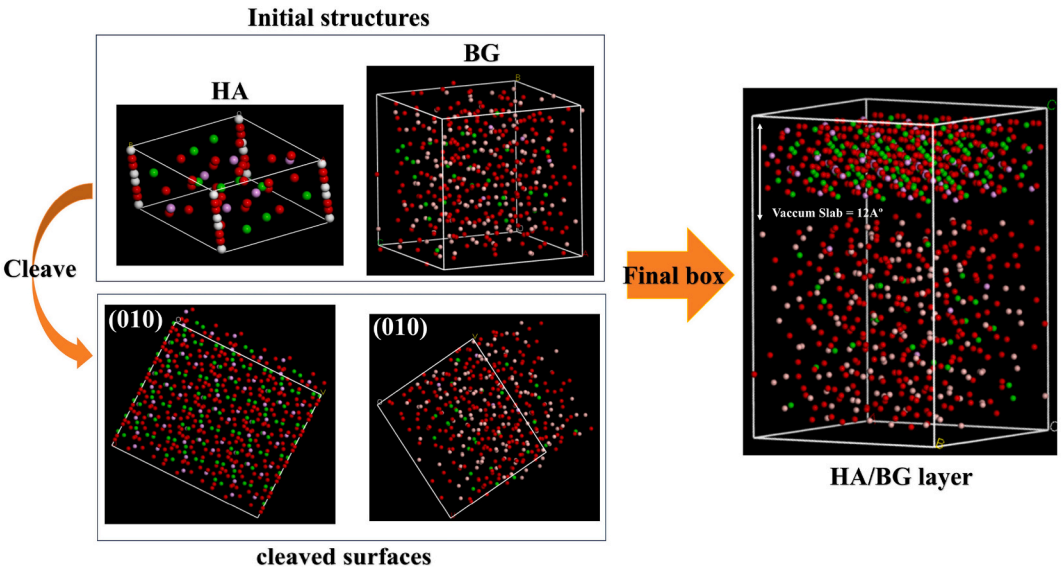

Fig. 4. Simulation of composite interface via molecular dynamics.

structure [13,14]. To control the process and bring the results closer to reality, the final simulated disordered atomic network of the glass was created with only the presence of the three principal oxides, B_2O_3, CaO, and P_2O_5, with the corresponding loading numbers of atoms. According to Fig. 4, the atomic network of borate glass (as a cubic arrangement for facility), called BG, can be seen. The software library also calls for the hydroxyapatite structure (HA). Moreover, the dimensions of the produced bulks of atoms had to be as close as possible to reduce any stress in the created networks. In this regard, the Lattice Parameter tool was first used to calculate and examine the dimensions of the initial networks of the two phases. According to this tool, the dimensions of the cubic glassy network are about 16A° in all three directions. In addition, the dimensions of the hexagonal hydroxyapatite cell in the x and y directions are approximately 9A°, and in the z-direction, they are about 6A°. The supercell tool available in the build tab is used to create convergence and relative agreement in both simulated bulks. With the help of this tool, the values of a, b, and c in the hydroxyapatite structure were grown with approximately corresponding coefficients. Furthermore, these two cells were subjected to stress relief and energy reduction operations to establish equilibrium and verify the stability in the resulting structures. In the next step, these two structures must be brought into contact to determine the bonding forces at contact and connection. Both simulated bulks are cleaved from one of their principal planes (010) to have the most incredible connection and establish coherence at the interface of the two phases [31]. Generally, the calculation of the phases' interface forces is necessary. Considering the disordered network of glassy phase, it must introduce an empty space for interfacial contact with ceramic structure in a larger area. Accordingly, the height of this area in the balanced state was considered to be about 12A°. Then, the second phase (ceramic structure) was added at the end of the designed space using the Build tool. According to Fig. 4, both layers were imported in the Build Layers > Defined Layers section and the final arrangement was created. This set must be examined spatially and energetically in the next step. Therefore, the Forcite module and the Geometry Optimization and Energy subprograms were used. In all stabilization stages, the Universal or COMPASSIII force field is used. Also, the quality of this simulation was set to Medium and Fine to prevent any errors in the simulation [32]. According to the Logfile data, the system's initial energy before stabilization was about 44171748.555437 kcal/mol, which reached −260527.133720 kcal/mol after equilibrium. The latter indicates a decrease in energy and proves the system's stability. After the set is stabilized, the molecular dynamics stage of this interface is examined. The molecular dynamics process specifications were selected according to the following path in the Forcite module to reach the system's equilibrium at ambient temperature.

Forcte > Setup > Task > Dynamics > More > Forcite Dynamics > Dynamics > Ensemble > NPT.

By selecting the NPT ensemble, the Nosé thermostat and Anderson barostat are chosen to keep the temperature and pressure conditions constant during the MD simulation.

In addition, the Ewald and atom-based method was used for the summation of the electrostatic and van der Waals forces. Also, the cutoff distance was set to 12.5 A°, and the buffer and spline widths were set to 2 A° and 1 A°, respectively [33]. By performing repeated simulations, the initial temperature was selected to be 300 K, and the simulation time was 100 ps. Afterward, the system's energy decreased to −618098.007 kcal/mol, indicating the equilibrium establization at ambient temperature.

ForciteDynamics > Dynamics > Ensemble > NPT.

According to previous studies and based on trial and error examinations, it was found that a time of 1000 ps and a temperature of 1000 K can provide suitable thermal conditions for simulation [34,35]. In other words, the tendency to form a composite and the interaction between two materials usually requires activation energy, which can be provided by increasing the temperature. It is worth noting that the timestep is equal to 1fs in all these steps, so the simulation has sufficient accuracy. As a result, the system's energy reaches the value of −127277.874 kcal/mol, indicating the increase in atomic fluctuations due to a slight temperature rise. Furthermore, the temperature was considered much lower than the glass melting temperature, which was about 4000K, based on a previous study to prevent any phase change or melting in both phases [33].

2.6. Calculation of density and molar weight of borate glass

In this study, the density of borate glass was calculated using Eq (3), and the final density value was calculated using the weight percentage of each component in the glass.

$$\rho_{glass} = \frac{100}{\sum \frac{w_i}{\rho_i}} \quad \text{Eq (3)}$$

In this equation, w_i and ρ_i are the weight percent and density of each oxide in the glass, respectively. Eq (4) was also used to calculate the molar weight of the glass. In this formula, M_i is the molar weight of each oxide in the final glass.

Table 2
Nominal ion concentrations of SBF in comparison with those in human blood plasma [39].

Ion	Ion concentration (mM)	
	Blood plasma	SBF
Na^+	142.0	142.0
K^+	5.0	5.0
Mg^{2+}	1.5	1.5
Ca^{2+}	2.5	2.5
Cl^-	103.0	147.8
HCO_3^-	27.0	4.2
HPO_4^{2-}	1.0	1.0
SO_4^{2-}	0.5	0.5
pH	7.2–7.4	7.40

$$M_{glass} = \frac{100}{\sum \frac{w_i}{M_i}} \quad \text{Eq (4)}$$

2.7. Method for calculation of crystalinity index (CI%)

The Crystallinity Index (CI) represents the ratio of regular (crystalline) to irregular (amorphous) parts in a material. One of the most accurate methods for calculating this index is to use the X-ray diffraction (XRD) pattern and analyze it using the peak deconvolution or area method. Unlike the simple Segal method, which uses only one peak and one amorphous point, this method considers the entire pattern. As a result, the results are more reliable [36]. In this regard, the XRD pattern of the sample was plotted within the appropriate angular range (in this study, 0–80°) using OriginPro 2024 (version: 10.1.0.178) software or a similar fitting software. After entering the data and plotting the curve in the software, baseline correction can be performed to reduce background noise. Next, the peaks are decomposed using the deconvolution operation. The angular region corresponding to the main peaks of the material is selected based on previous phase determinations and reference XRD codes. It is noteworthy that the main peaks of the hydroxyapatite phase were identified in the selected samples. The percentage of total crystallinity relative to the total material and other phases (if present) was then calculated. After this step, the fitting of the patterns was performed using mathematical functions, such as the Gaussian function. The area range of each peak was also selected with the smallest width to increase accuracy. Then the area under the determined peaks was calculated. The total area of the determined peaks is divided by the total area under the curve and multiplied by 100. The resulting number is the crystallinity index [37,38].

2.8. Characterizations

The samples were analyzed using an *EXPLORER G.N.R. S.r.l (GNR) (Novara, Italy)* X-ray diffractometer to investigate the crystalline phases. Cu-Kα radiation (λ = 1/540598 Å) was used at a voltage of 40 kV, in the 2θ range from 15 to 80° at room temperature and a scan step of 0.05°. To understand the morphology and microstructure of the samples, a *TESCAN BRNO-Mira3 LMU* FESEM microscope with an accelerating voltage of 15 kV, coupled with energy dispersive X-ray spectroscopy (EDX), was used for the purpose, as well. To obtain the most accurate results, the FESEM samples were subjected to gold plasma coating for 15 min to allow observation of the microstructure in non-conductive ceramic systems. Particle size analysis was performed using a *Vasco3 CORDOUAN* device to determine the particle dimensions. In the particle size evaluation, 0.01 g of each sample powder was dispersed in ethanol and then placed in an ultrasonic bath for 30 min to achieve maximum particle distribution. A *LEO* 912AB transmission electron microscope (TEM) with an operating voltage of 120 kV was used to examine nanoparticle size, shape, dispersion, and structures in the optimized composite powders. For sample preparation, 0.01 g of powder was mixed with 30 mL of pure alcohol and sonicated (using *FR USC 22 LQ, 400 W, 20 % Taiwan*) for 10 min. After that, a drop of the resulting suspension was applied to a standard carbon-coated copper mesh for TEM analysis. Also, several microscopic images were recorded using an optical microscope to examine the surface of the composite tablets obtained from SPS and observe the phases present on the sample surface. A microhardness tester (*Matsuzawa, MHT2-Japan*) was used to measure the hardness index in the pressed samples accurately. In this regard, at least 16 indentations were considered to have an average microhardness value for each composite sample. Also, a *Thermo Nicolet AVATAR* 370 FT-IR instrument, a reliable Fourier transform infrared (FT-IR) analyzer, was used to identify the functional groups produced during the initial synthesis and SBF immersion processes. The analysis consisted of 32 scans, performed throughout 40s, with a resolution of 4 cm^{-1} and a pressure of 8 GPa. The particles were created by grinding approximately 1–2 % of the powders with KBr solution in the 400-4000 cm^{-1} range. The ratio of KBr to synthesized powder for FTIR analysis was approximately 99:1. In addition, atomic force microscopy (AFM) was used to analyze the tablets' surfaces after dry conditions and 28 days of immersion. The technique employed was phase imaging, which detects cantilever phase changes for topographic mapping and material differentiation. This method is beneficial for studying polymers, composites, and surface coatings. Images were acquired using a *FlexV5+ Scanhead* with a controller operating in phase imaging mode at 158.614 kHz, and a vibration amplitude of 1.5 V. Image analysis was performed using Mountain Maps software.

2.9. Characterizations after exposure to simulated body fluid (SBF)

Initially, simulated body fluid was prepared to investigate the biological behavior of the tablets according to the formula introduced by Kokubu [39]. Table 2 shows the SBF ion concentration in comparison to blood plasma. Afterward, the composites were divided into smaller parts of equal weight and placed in a certain amount of SBF solution. These samples containing solutions were kept in a shaking incubator for periods of 3 h (3h), 1 day (1D), 3 days (3D), 7 days (7D), 14 days (14D), 21 days (21D) and 28 days (28D). After the desired periods, the samples were removed from the solution and washed with ethanol to prevent any biological reaction after leaving the SBF. Also, they were dried at room temperature. ICP-OES (inductively coupled plasma optical emission spectroscopy) analysis used an Arcos Spectra device to examine the release rate and ion-exchanged during immersion. To investigate the mechanical properties of the obtained tablets, diametral tensile strength (DTS) test was used. Then, each sample was examined for both dry conditions and 28-day immersion in SBF to ensure the impact of the environment on DTS values. This test was performed at a test speed of about 0.2 mm/min and a gage length of 150 mm. These parameters were selected based on previous studies to enhance accuracy and mitigate the effects of rapid loading rates on synthesized HA/BG tablets [40–42]. The objective was to enhance measurement repeatability and to better control the test's dynamic aspects. After testing, the following equation (Eq (5)) was used to calculate the diagonal tensile stress (σ_t) from the measured fracture force (P):

$$\sigma_t = \frac{2P}{\pi DL} \quad \text{Eq (5)}$$

This formula is standard in Brazilian tensile test studies for brittle or semi-brittle materials. Here, σ_t is the diagonal tensile stress (MPa), P is the fracture force (N), D is the specimen diameter (mm), and L is the specimen thickness (mm) [43]."

Table 3
Calculations of the adiabatic temperatures for the reactions conducted.

Sample code	T_{ad} (K)	Sample code	T_{ad} (K)
100 %BG-P	1166.5	100 %HA-P	1315.5
20 %HA-II-P	1163.3	80 %HA-I-P	1261.3
25 %HA-II-P	1162.5	75 %HA-I-P	1245
50 %HA-II-P	1155.5	50 %HA-I-P	1149
75 %HA-II-P	1141.3	25 %HA-I-P	1112
80 %HA-II-P	1136.7	20 %HA-I-P	1109.4

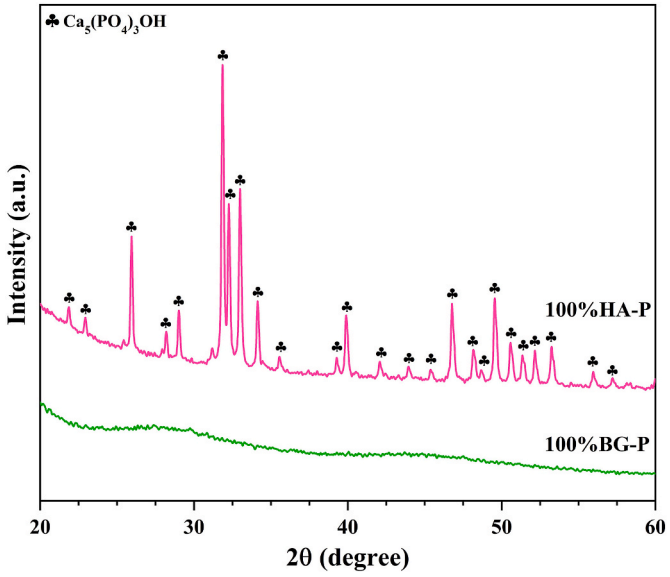

Fig. 5. XRD results obtained from pure powders of hydroxyapatite (HA) and borate glass (BG).

3. Results and discussion

3.1. Thermodynamics calculation

Thermodynamic calculations play a crucial role in understanding the influence of various effective parameters on chemical reactions. In solution combustion synthesis, a key aspect is calculating the adiabatic temperature (T_{ad}) using thermodynamic principles, as highlighted in Eq (6). T_{ad} is a theoretical index calculated assuming a closed chamber (adiabatic conditions) [44].

$$-\Delta H_f^0 = \int_{T_0}^{T_{ad}} \sum C_{P(products)}\, dt \qquad \text{Eq (6)}$$

Accordingly, C_P is the specific heat at constant pressure, and $-\Delta H_f^0$ is the standard enthalpy of the reaction.

Furthermore, Table 3 represented the adiabatic temperature (T_{ad}) in different HA: BG weight ratios. Based on calculations, the adiabatic temperature for pure HA was about 1315.5 K. Adding different wt.% of BG to the HA initial solution could also affect T_{ad} (via method I). According to the results, Tad has decreased with increasing BG content. The temperature decreasing trend continued up to 200 K in the 20 %HA-I-P sample. This significant decrease in temperature prevented the complete synthesis of HA in the presence of BG particles. Besides, T_{ad} is about 1166.5 K for pure BG. Adding the different wt.% of HA in the initial BG solution decreased T_{ad} by about 30 K, which could be tangible compared to method I. Therefore, the effect of the BG as secondary phase has been more significant. As derived from calculations, the molar weight of BG is about 67.13 g/mol, and it is about 502.31 g/mol for HA. Hence, this difference can be attributed to fewer HA moles than BG in a specific weight. Notably, higher molar weight caused less reactive and more uniform heat distribution in the system [45].

3.2. Powders characterizations

3.2.1. XRD results of pure hydroxyapatite and borate glass powders

Fig. 5 illustrates the X-ray diffraction patterns for pure HA and BG powder. Due to the glass's amorphous nature, the XRD pattern of 100 % BG-P demonstrated no characteristic peaks [46]. In other words, the lack of lattice order leads to non-uniform X-ray diffraction [47]. Unlike 100 %BG-P, the prominent characteristic peaks in 100 %HA-P are visible (2θ = 25.9°, 31.8°, 32.7° and etc) identified as $Ca_5(PO_4)_3OH$ (ICDD card 00-034-0010). Additionally, the crystallinity index (CI) of 100 %HA-P is about 91 % due to the formation of some amorphous (undeveloped) phases in the low-angle region of the diffraction pattern [48].

3.2.2. XRD results of composite powders

The XRD diffraction patterns of the composite powders synthesized by method I (adding BG particles into the HA solution) and II (adding HA particles into the BG solution) are illustrated in Fig. 6(a) to 6(e), respectively. Based on the shown spectra, the percentage of the glass phase gradually increased with decreasing HA content. The characteristic peaks of hydroxyapatite (ICDD 00-034-0010) are identifiable as the predominant formed phase in both groups of samples. As shown in Fig. 6 (a), the characteristic peaks of $Ca_5(PO_4)OH$ (ICDD card 00-034-0010) are evident in both the 80 %HA-I-P and 75 %HA-I-P samples, indicating the primary crystallized phase. The stronger characteristic peaks in the 75 %-I-P compared to the 75 %-II-P, suggest a greater tendency to form HA as showed in Fig. 6(c). Moreover, the slightly uneven background is attributed to the presence of the minor glass content [49]. The observations indicate that the increasing in the BG content in samples of 20 % HA-I-P, 25 % HA-I-P, and 50 % HA-I-P caused an amorphous trend with several crystallized phases. These phases include $Ca_2P_2O_7$ (ICDD 00-003-0605), KH_2PO_4 (ICDD 01-072-1021), and $Na(PO_3)_3$ (ICDD 00-001-0653). Based on the thermodynamic calculations, the presence of BG leads to a reduction in T_{ad} (Table 3). This reduction caused a decrease in solution homogenity via easier ion diffusion [13]. This reduction in solution homogeneity could change the calcium-to-phosphorus ratio and cause the formation of additional phases. Consequently, the incomplete synthesis of the HA phase occurred in samples with higher BG content. As mentioned earlier, the crystallinity index of pure HA was about 91 %. Hence, the absence of HA characteristic peaks can be attributed to the formation of amorphous hydroxyapatite. Only the samples with crystalized HA were studied to investigate the crystallization index (CI) further via method I. As a result, the crystallinity index was calculated to be 63 % and 68 % for the two samples, 80 %HA-I-P and 75 %HA-I-P, respectively in Table 4. In this regard, the 75 %HA-I-P sample was selected as optimal for subsequent analyses due to the coordination of the same calculated and experimental crystallinity levels. Unlike the previous method, the diffraction patterns of method II demonstrate the HA crystalization, as illustrated in Fig. 6(b). Via method II, HA particles disperse in the BG solution that prevent the solution ions to be correlated. This is due to the ability of HA particles to absorb heat, which reduces the rate of exothermic reactions and delays the synthesis duration [50]. Moreover, the similar ions between BG and HA could cause ion exchange. Hence, several characteristic peaks related to the crystallization of secondary phases, including β-TCP (ICDD 00-009-0348), $CaHPO_4$ (ICDD 01-071-1760), KNO_3 (ICDD 01-074-1198), and a minor presence of boric acid (H_3BO_3, ICDD 00-030-0620) are also evident. For example in Fig. 6(d), the presence of additional and two-branches peaks in 75 % HA-II-P indicate possible undesirable phases formed during method II, compared to 75 %HA-I-P that proved the latter criteria. In the 75 % HA-II-P sample, and more generally in method II, pre-prepared hydroxyapatite (HA) particles are added to the 13–93B3 bioactive glass (BG) synthesis solution, so the BG phase forms while HA is present. As

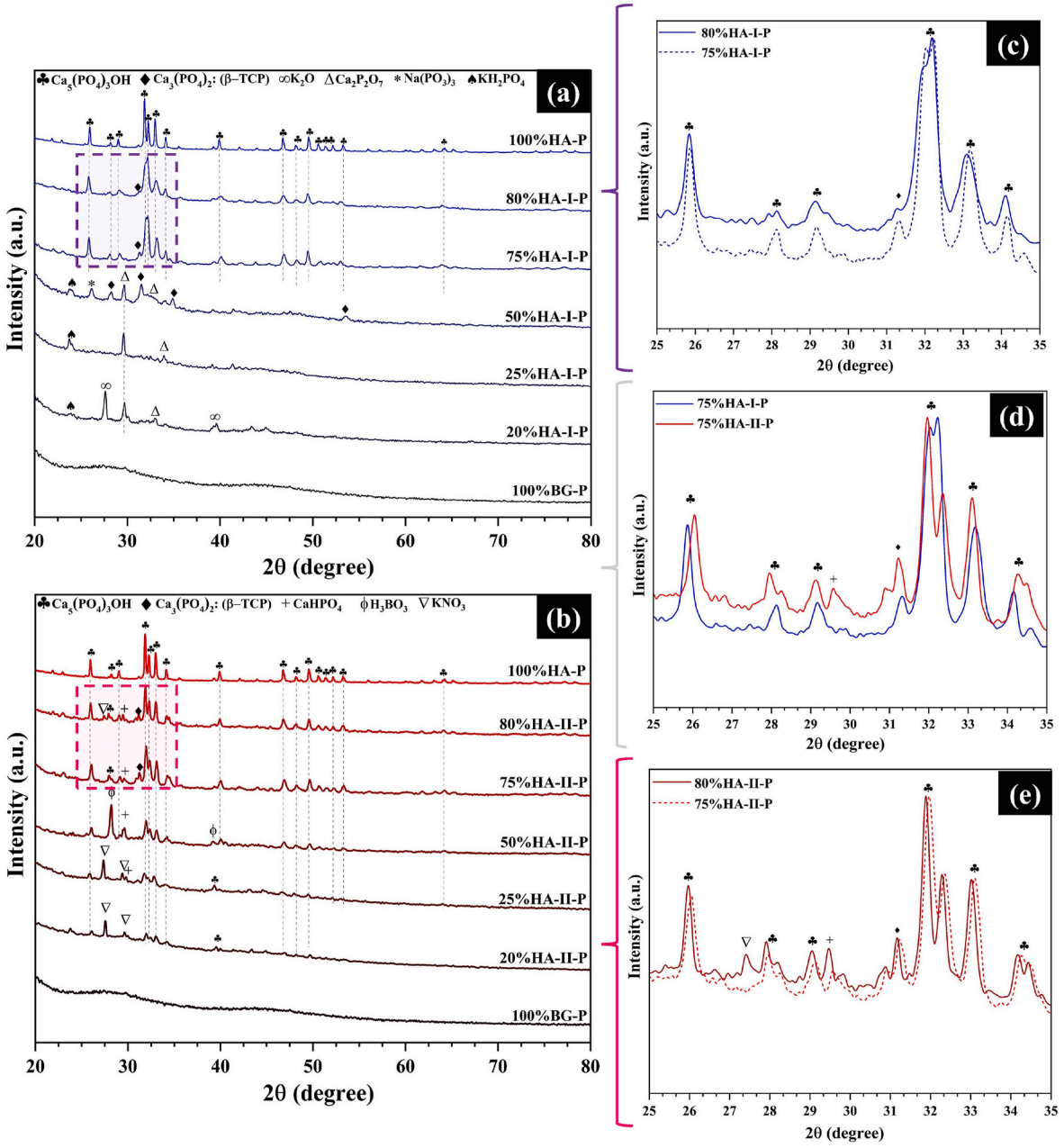

Fig. 6. XRD analysis of composite powders in both (a) methods I & (b) method II, (c) and (e) the comparison of 80 %HA and 75 %HA in two methods, (d) both optimal samples.

Table 4
Comparison of the crystallization index (HA phase) using computational and experimental methods in samples of method I.

Samples (Method I)	Crystallization Index (hydroxyapatite phase) (%)	
	Computational	Experimental
80 %HA-I-P	91 % × 80 % = 72.8	~63
75 %HA-I-P	91 % × 75 % = 68.25	~68

Table 5
Crystallization Index in composite samples from synthesis method II determined by experimental methods excluding HA.

Samples (Method II)	Crystallization Index (excluding hydroxyapatite) (%)
80 %HA-II-P	~8
75 %HA-II-P	~5
50 %HA-II-P	~19
25 %HA-II-P	~18
20 %HA-II-P	~17

mentioned earlier, method II can lead to side phases due to ionic displacement, the heat absorption of the HA phase, and the lower stability of the BG solution when HA particles are present. Earlier studies have shown that increasing the solution temperature can activate the HA phase, allowing scattered ions to replace those in the (002) crystal plane of HA, which has a characteristic diffraction angle at 25.9° [51,52]. The (002) plane refers to a specific orientation in the HA crystal lattice. If smaller ions take their place, the distance between these planes (called d-spacing) gets smaller. According to the Bragg's equation ($n\lambda = 2d\sin\theta$, where λ is the wavelength of the X-rays, d is the spacing between planes, and θ is the diffraction angle), a smaller plane distance means the angle θ gets larger, so the peak moves to higher angles [53,54]. The observed peak shift in a certain plane and angle suggests that the HA phase

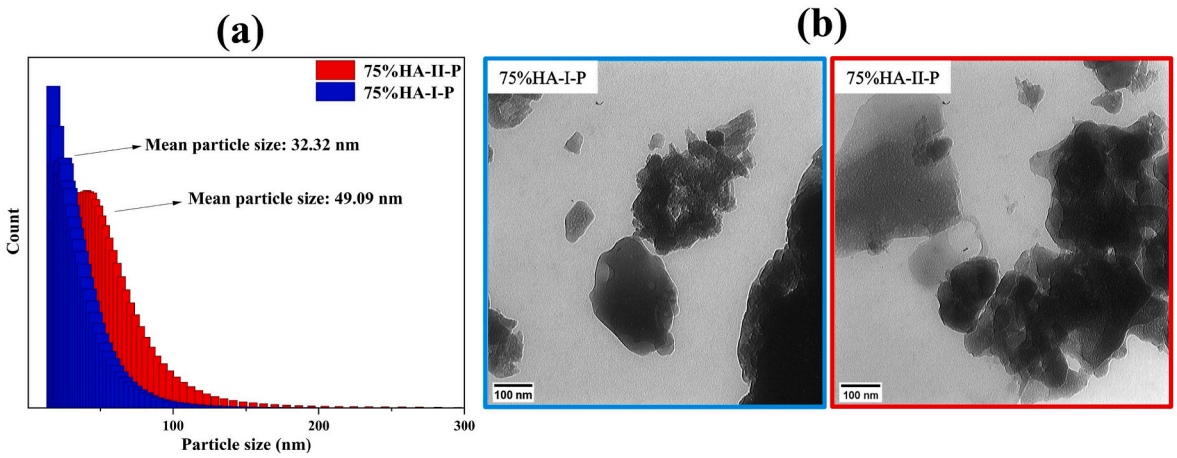

Fig. 7. PSA and TEM results of the optimal samples.

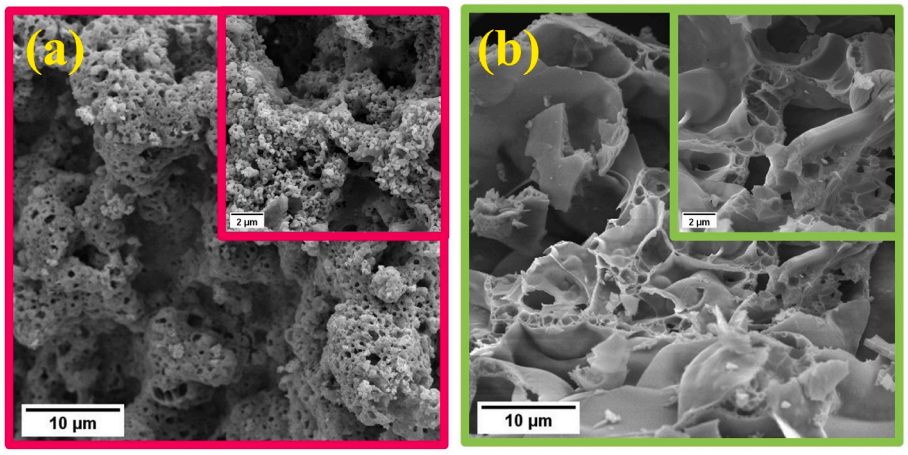

Fig. 8. FESEM results of samples of a) pure hydroxyapatite (100 %HA-P) and b) pure borate glass (100 %BG-P).

remains stable even with BG solution, indicating that there is only a small amount of doping with the new ion, and the original HA crystal structure is preserved. As mentioned earlier, the crystallization of HA in all samples via method II leads to a crystallization index that should meet or exceed calculated values. Therefore, Table 5 compares the crystallinity index of secondary phases (except HA). Furthermore, Fig. 6 (e) indicates that the presence of undesirable phases was reduced in the sample 75 %HA-II-P. Due to the resulting data, the 75 %HA-II-P sample has the lowest impurity phase (5 %) that was selected as the optimal sample.

3.2.3. PSA and TEM results of optimal composite powders

PSA and TEM analysis (as shown in Fig. 7) were used to investigate the particle size and morphology in the two optimized samples. According to the data, the D50 index in the 75 % HA-I-P sample is about 68 nm with an average particle size of 32 nm, and in the 75 % HA-II-P sample is about 89 nm with an average particle size of 49 nm. The observed difference can be attributed to the various adiabatic temperatures. As previously mentioned, the T_{ad} for the synthesis of 75 %HA-I-P was about 1245K, and it is 1141.3K for 75 %HA-II-P. In a study conducted by Sun et al. (2018) [55], the researchers investigated how the content of ceramic particles and the adiabatic temperature affected the porosity of composites during solution combustion synthesis process. The findings indicated that increasing the adiabatic temperature led to a reduction in the final particle size. Consequently, the increased Tad during the synthesis of 75 %HA-I-P results in a reduced particle size in comparison to that observed in the 75 %HA-II-P synthesis. Another aspect could be the types of the secondary phase (HA and BG phase) introduced into the initial synthesis solution through methods I and II. The initial HA powders, using method I, have an average particle size of about 68 nm, according to the experiments [56]. Therefore, the initial nuclei are considerably larger. This is primarily due to their enhanced stability, which reduces surface dissolution when exposed to the BG solution. However, this phenomenon differs from method II due to the higher energy level and a faster dissolution rate with BG particles (with an average particle size of 67 nm [13,14]). Therefore, crystal nuclei restrict nucleation to specific locations at a lower rate [57]. According to the TEM images in Fig. 7(b), two microstructures are observable. Based on the findings from FESEM analysis, it can be inferred that agglomerates exhibiting elevated surface roughness may be linked to hydroxyapatite (HA) particles [58,59]. Besides, the BG phase appeared as discontinuous plates [60].

3.2.4. FESEM results of composite powders

The FESEM images of pure HA and BG powder are displayed in Fig. 8. The presence of pores in HA's microstructure is likely due to gas release phenomen during the synthesis process [61]. The observation of interconnected structures [56] in Fig. 8(a) primarily arises from HA's crystalline nature, which facilitates the arrangement and aggregation of particles cohesively [62]. Moreover, Fig. 8(b) shows several discontinuous plates in the microstructure of BG, which occur due to its disordered nature.

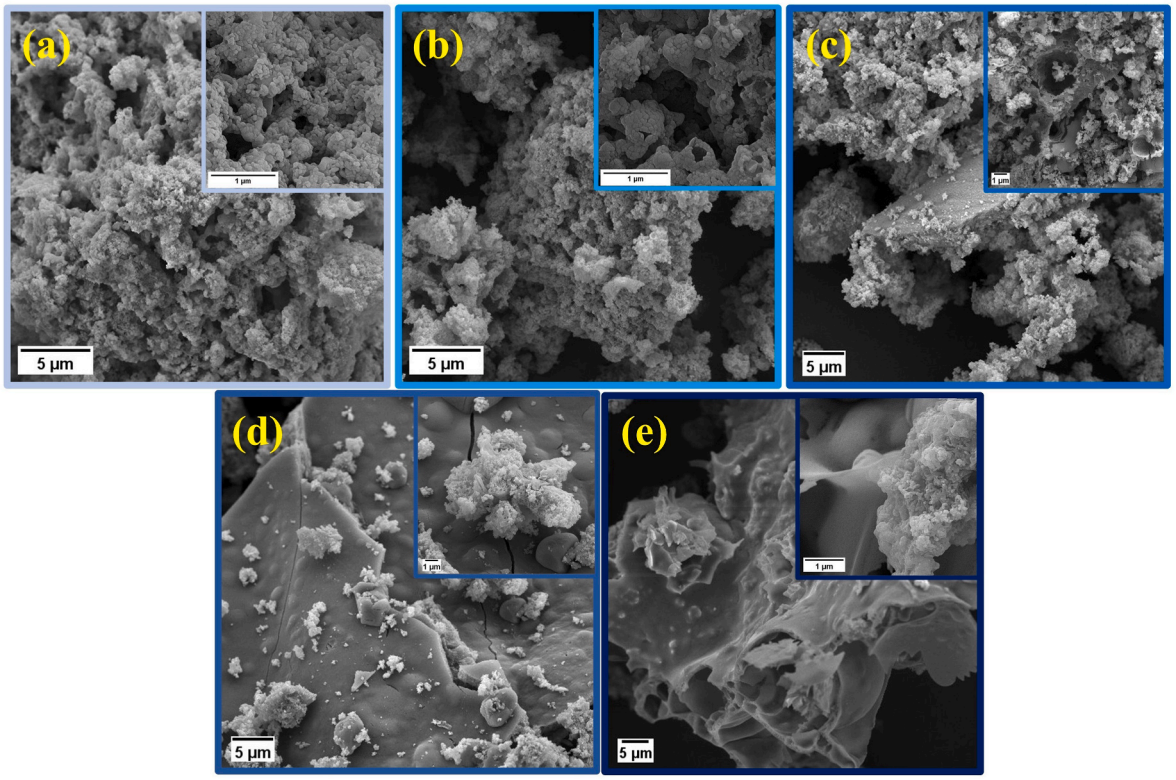

Fig. 9. FESEM results of composite samples containing borate glass powder/hydroxyapatite solution: a) 80 %HA-I-P, b) 75 %HA-I-P, c) 50 %HA-I-P, d) 25 %HA-I-P and e) 20 %HA-I-P.

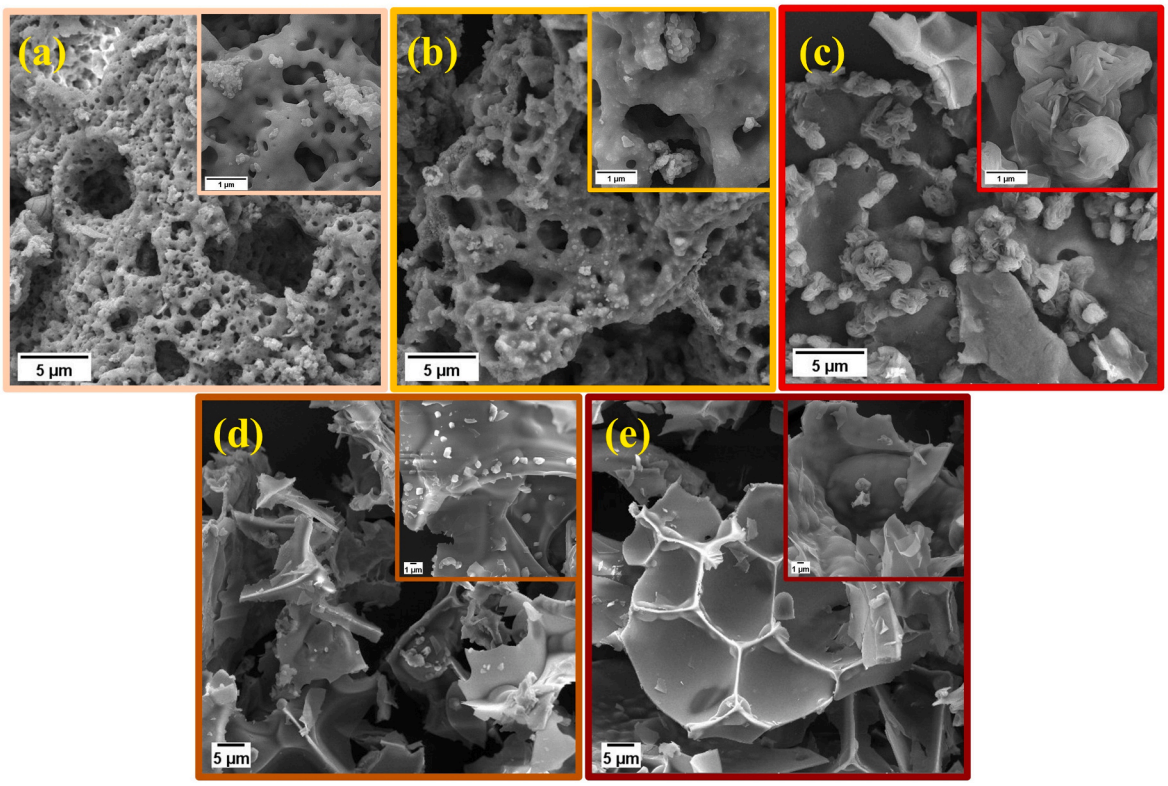

Fig. 10. FESEM results of composite samples containing hydroxyapatite powder/borate glass solution: a) 80 %HA-II-P, b) 75 %HA-II-P, c) 50 %HA-II-P, d) 25 %HA-II-P and e) 20 %HA-II-P.

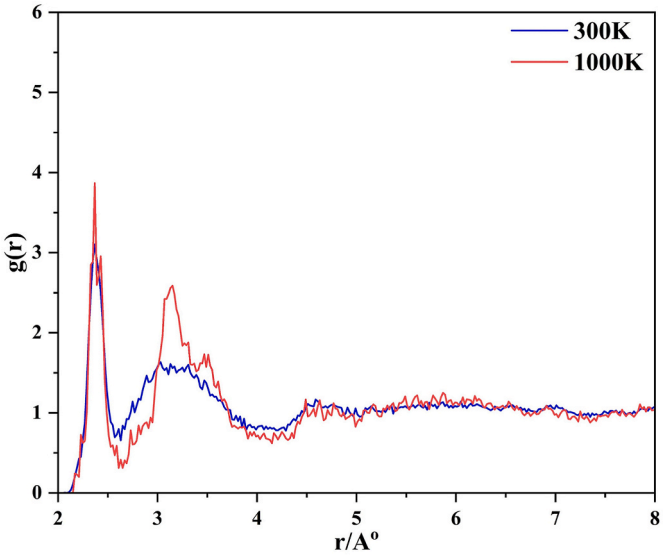

Fig. 11. Radial distribution function (RDF) results of molecular dynamics simulation.

Table 6
Volume percentages of borate glass and hydroxyapatite phases in analyzed samples.

Samples (HA:BG) weight content	Phase volume (%)	
	13–93B3 glass	Hydroxyapatite
80 %HA:20 %BG	~23	~77
75 %HA:25 %BG	~29	~71
50 %HA:50 %BG	~55	~45
25 %HA:75 %BG	~78	~21
20 %HA:80 %BG	~83	~17

Fig. 9 illustrates the FESEM results for the samples via method I. In high HA content samples, HA porous microstructure prevents the appearance of the BG phase [63]. The BG plates become more evident by reducing the HA content from Fig. 9(a)–(e). Due to the observed microstructure as Fig. 9(c), the pre-prepared BG phase is expected to act as the initial place for the nucleation of the HA solution. In other words, the HA phase is expected to grow from the surface of the BG phase. Finally, the sample 20 %HA-I-P consists entirely of BG plates with several points of HA's agglomerates [14].

Fig. 10 shows the FESEM images of the composite powder via method II. From Fig. 10(a)–(e), the microstructure has transformed into discontinuous plates with increasing BG content. In lower BG content samples, the porous HA phase acts as the nuclei for the glass solution. Therefore, an interconnected glassy network will likely cover the HA agglomerates [59]. The mentioned network will vanish via reducing HA content and be transformed into BG plates.

3.2.5. *Molecular dynamics simulation results*

The results of the simulation (RDF results) are illustrated in Fig. 11. According to experimental procedure of simulation, the system's total energy remains negative even after a slight increase in temperature. This stability of the system's energy indicates equilibrium and the tendency of the two phases to mix with each other in control sample [32,34,35]. In addition, RDF analysis was used to investigate this tendency to combine. Radial distribution functions (RDFs) and coordination number (n) indicate the probability of distribution of selected particles in a spherical space around a given particle. They are usually used to describe the distribution of the system network and the degree of disorder. The corresponding calculation formula (Eq (7)) is shown below:

$$g(r) = \frac{V}{N}\frac{n(r, dr)}{4\pi r^2 dr} = \frac{\sum_{t=1}^{T}\sum_{j=1}^{N}\Delta N(r \rightarrow r + dr)}{T \times N} \quad \text{Eq (7)}$$

In this formula, V is the volume of system. N is the number of atoms, n(r, dr), ΔN refers to the number of atoms in the radius range from r to r + dr, and T is the simulation time [32].

According to Fig. 11, the total bulk at 300K tends to value of 1 after showing several peaks. In other words, no apparent order is far from the hypothetical atom. This proves the simultaneous order/amorphism of the resulting composite. In addition, the system shows more intense peaks with a slight increase in temperature. In other words, if the two powders are perfectly compatible, the atomic peaks at the interface will display a less-noisy pattern. Otherwise, the interface peaks will be small or absent if the interaction is weak. Intense peaks at certain distances

Table 7
The microhardness values of the three optimal tablets after SPS.

No.	Sample	Microhardness values
1	75 %HA-I-T	68 ± 19 Hv
2	75 %HA-II-T	151 ± 39 Hv
3	75 %HA-III-T	143 ± 105 Hv

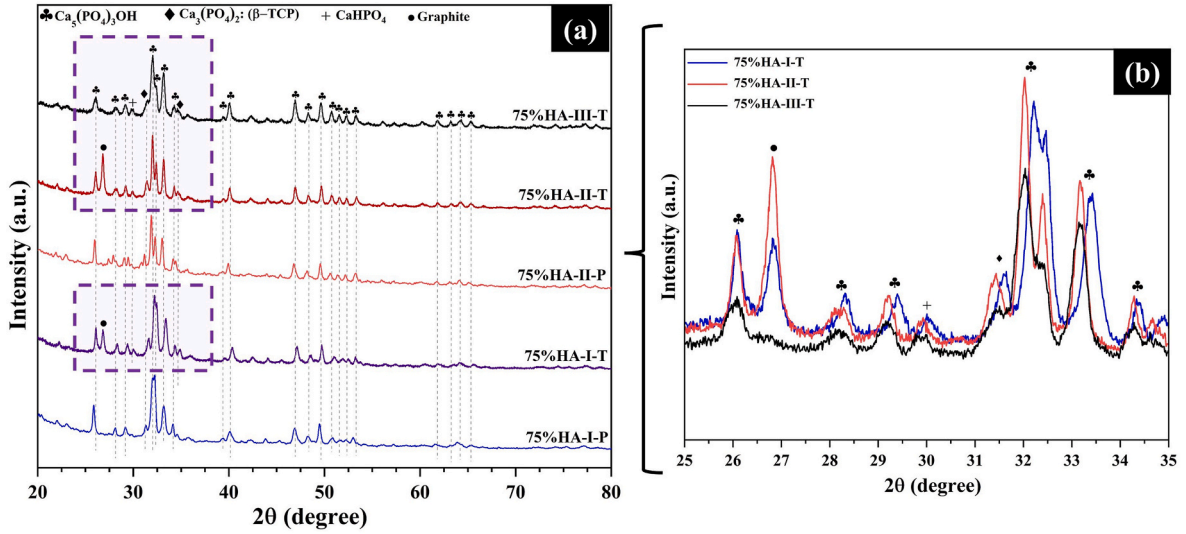

Fig. 12. (a) The results of tablets XRD characterization after SPS procces, (b) The comparison of three optimal tablets.

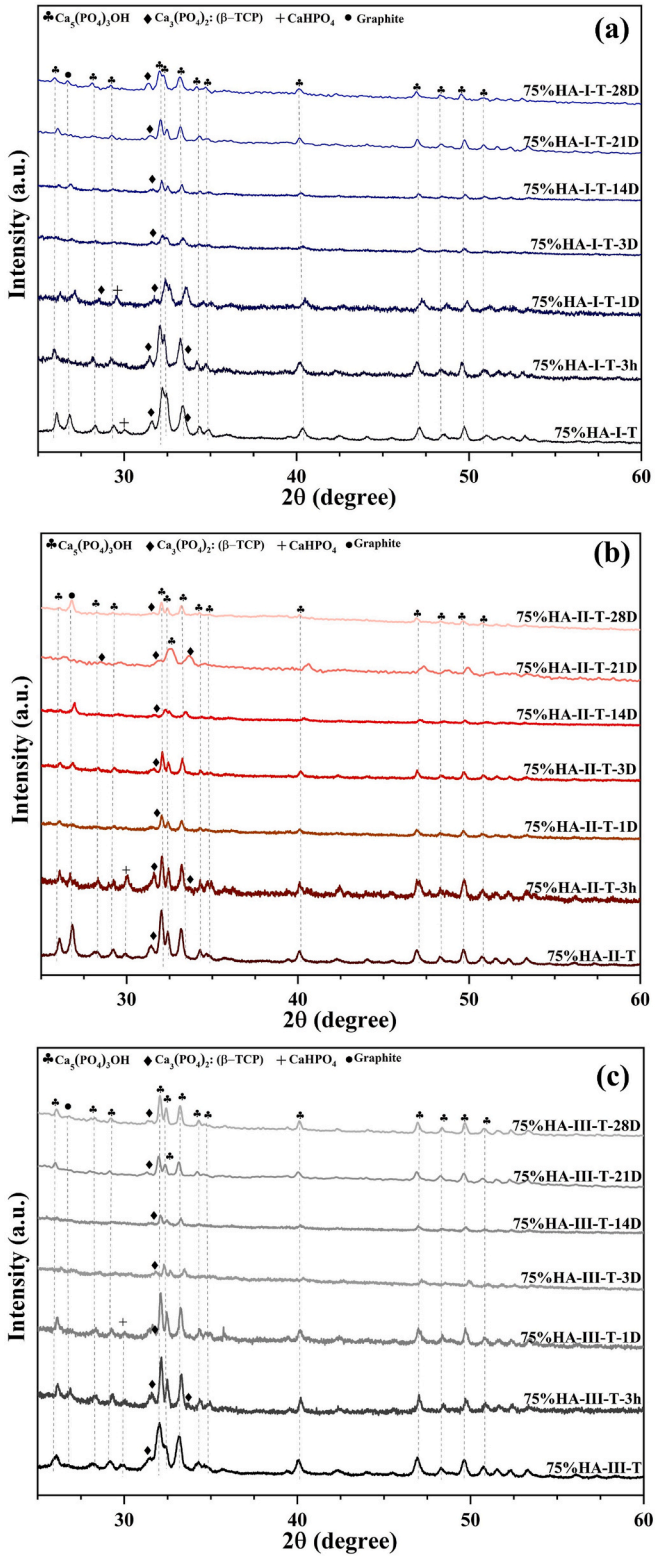

Fig. 13. XRD patterns of samples after immersion in SBF: (a) 75 %HA-I-T, (b) 75 %HA-II-T and (c) 75 %HA-III-T.

indicate a strong bond at the interface. In contrast, if the interface is weak, the radial distribution function (g(r)) at small radii will immediately approach the value 1, indicating a uniform density. Furthermore, the intensity of the peaks increases as the temperature rises. This indicates the inhibition of the selected temperature from forming unwanted phases due to melting. It also shows that the system tends to be ordered with increasing atomic mobility [33,34,64]. For more validation, the values extracted from RDF before and after simulation have been examined for two different bonds at the initial temperature and 1000K. The first atomic bond is related to calcium and oxygen ions on the hydroxyapatite surface, whose peak radius is 2.83A° and 3.43A° at 300K and 1000K, respectively. The second bond is related to calcium ions on the hydroxyapatite surface and oxygen ions on the glass cross-sectional surface, whose first peak radius is 5A° and 4.69A° at 300K and 1000K, respectively. A reduction in the distance between oxygen ions from glass and calcium ions from hydroxyapatite, resulting from increased temperature, together with a greater separation between oxygen and calcium ions at the hydroxyapatite surface, suggests a propensity for composite formation. In other words, the first peak RDF curves indicates the distance of the closest particle to the hypothetical particle. The lower this peak is located at x values, the shorter the distance between the selected and secondary particles [34,64,65].

3.3. Tablets characterizations after SPS

In order to investigate the impact of the synthesis method on the final properties, an optimal amount of BG and HA powders were physically mixed and subjected to SPS technique (as sample 75 %HA-III-T). Since 13–93B3 bioactive glass and hydroxyapatite have similar densities (2.59 and 3.16 g/cm^3) and comparable weight/volume percentages, the risk of phase separation is minimal. This supports the use of a straightforward mixing approach for the control sample. Research shows that when phases have similar volume and weight, simple mixing methods, such as hand milling, yield a uniform distribution, making high-energy techniques unnecessary [9,10]. This is supported by the comparison of volume and weight percentages as illustrated in Table 6. While high-energy methods can improve mixing, they may also cause problems such as contamination or unintended changes in the material [66,67]. Considering the similar physical properties and these findings, a low-energy mixing method is both effective and preferable. Furthermore, simulations were performed and confirmed the possibility of the two phases to form stable interfaces and supporting the use of simple mixing for the composite. As a result, the XRD patterns of the optimized composite (75 % HA) in powder and tablet form are shown in Fig. 12(a). The results indicate that the primary phases formed remained consistent, even following the SPS process. In other words, The visible result of XRD suggested that the SPS process was deemed only to enhance the existing peaks. Considering the lower glass proportion compared to HA content, there may be some minor phases from reactions between HA and BG. These may be present in the sub-limit of XRD measurements and could not be observed in the present data [26,68,69]. As shown in Fig. 12(b) samples 75 %HA-I-T and 75 %HA-II-T illustrated more intense peaks related to HA. It could be attributed to the synthesis of one phase in the presence of particles of another phase in method I and II. Also, due to the partial penetration of the graphite layer covering the powders in the SPS process, a visible peak corresponding to graphite (COD 96-901-1578) at $2\theta = 26.6°$ appeared after the SPS process. In the following, the microhardness values of the optimized tablets are presented in Table 7. For the 75 %HA-III-T sample, the hardness value changes at a wider range, suggesting a heterogeneous surface, unlike the other two samples. This nonuniformity is attributed to the synthesizing method and the separate initial powders of BG and HA phases [1, 70–73]. According to the results, the average hardness values are 68 ± 19 Vickers for the 75 %HA-I-T sample, 151 ± 39 Vickers for the 75 % HA-II-T sample, and 143 ± 105 Vickers for the physically mixed sample. Additionally, the larger range of changes (±105 units) in control sample, indicating its lower homogeneity compared to the other two samples [74]. Accordingly, the difference in hardness values between the two in-situ synthesized samples can be due to the size of the initial composite powder. In other word, the increment in specific surface area via smaller particles in the SPS, the resulting weaker sites reduce surface hardness. Furthermore, Estey et al. [75] found that the average hardness range for

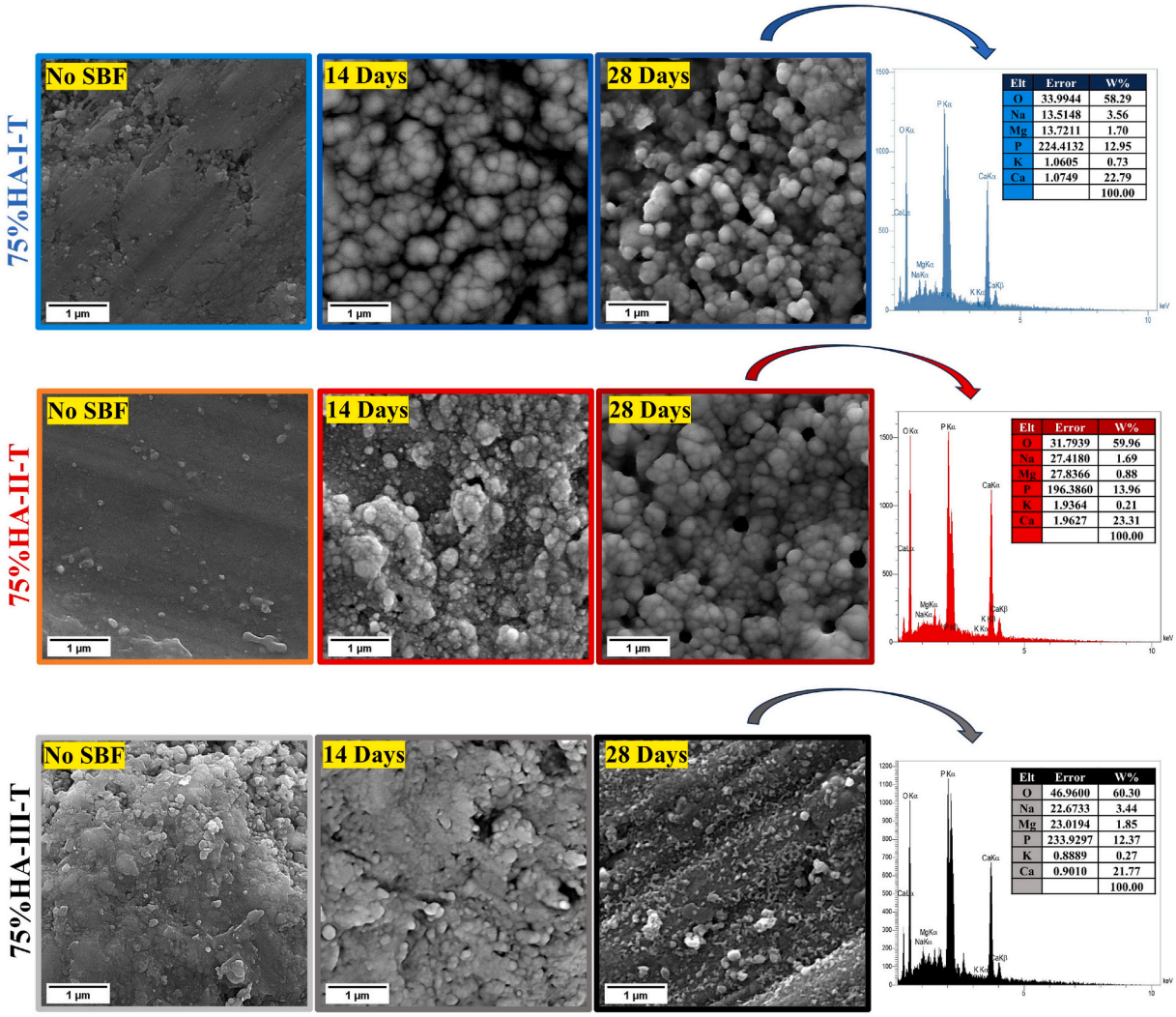

Fig. 14. FESEM imges of samples after immersion in SBF for different time intervals with the results of EDX after 28 days immersion.

the condensed parts of the bone is about 50–60 Vickers. Hence, the 75 % HA-I-T sample can be introduced as a proper substitution for damaged bone due to the hardness value.

3.4. Tablets characterizations after immersion in SBF

3.4.1. XRD results of SBF-immersed tablets

Fig. 13 represents the XRD patterns of composite tablets used to investigate the effect of immersion in the simulated body fluid (SBF) after different time intervals. While the samples showed intense, prominent characteristic peaks related to the HA phase (ICDD 00-034-0010), the others showed a reduction in the intensity of the HA characteristic peaks after immersion in SBF. In other words, the intensity of the HA characteristic peaks decreases as immersion time increases. The BG presence in the final composite affects the sample release rate in SBF and helps improve the biological performance of the sample [13,14,26]. Moreover, patterns showed a continuous trend of surface dissolution until the first or third day of immersion. At the same time, new phases formed on the sample surface, which can be crystalline or amorphous due to their formation rate [63]. According to previous studies, bone formation consists of two main processes-surface ion release and simultaneous precipitation of Ca^{2+} and PO_4^{3-} that form a mineral layer on the sample [21,26,76]. Therefore, the formation of an initial hydroxyapatite phase on the surface that is not entirely crystalline and requires time to crystallize is expected [77]. Besides, a characteristic peak related to the $CaHPO_4$ (ICDD 01-071-1760) transform to HA phase over time [78]. Additionally, low-intensity graphite characteristic peaks emerged from the SPS process preparation.

In the following, a comparison is presented among three samples. As immersion time passes, 75 %HA-I-T and 75 %HA-II-T samples show rapid ion dissolution at the first stage. Then, the surface mineralization begins and continues until 28 days of immersion. However, the 75 %HA-III-T sample underwent a longer demineralization process. This is attributed to its initial synthesis method. In other words, the separate presence of pre-prepared powders of BG and HA caused the creation of individual islands, ultimately showing the heterogeneous dissolution in SBF [1,70,79]. Also, the 75 %HA-III-T pattern after 28 days of immersion is observed to have more intense HA peaks than the others. It could be considered a greater mineralization rate and a better biocompatible performance. In addition, the precipitated HA phase on the surface is initially amorphous and crystallizes upon prolonged exposure to the SBF [77]. Therefore, for a precise investigation from a microstructural perspective, the results of FESEM are demonstrated below.

3.4.2. FESEM results of SBF-immersed tablets

The FESEM results of the 14 and 28 days SBF immersed samples are shown in Fig. 14. According to these results, the influence of the synthesis method on the bioactivity of the samples could be observable. According to figures after 14 days of immersion, the two produced in-situ composites displayed several agglomerates in their morphology

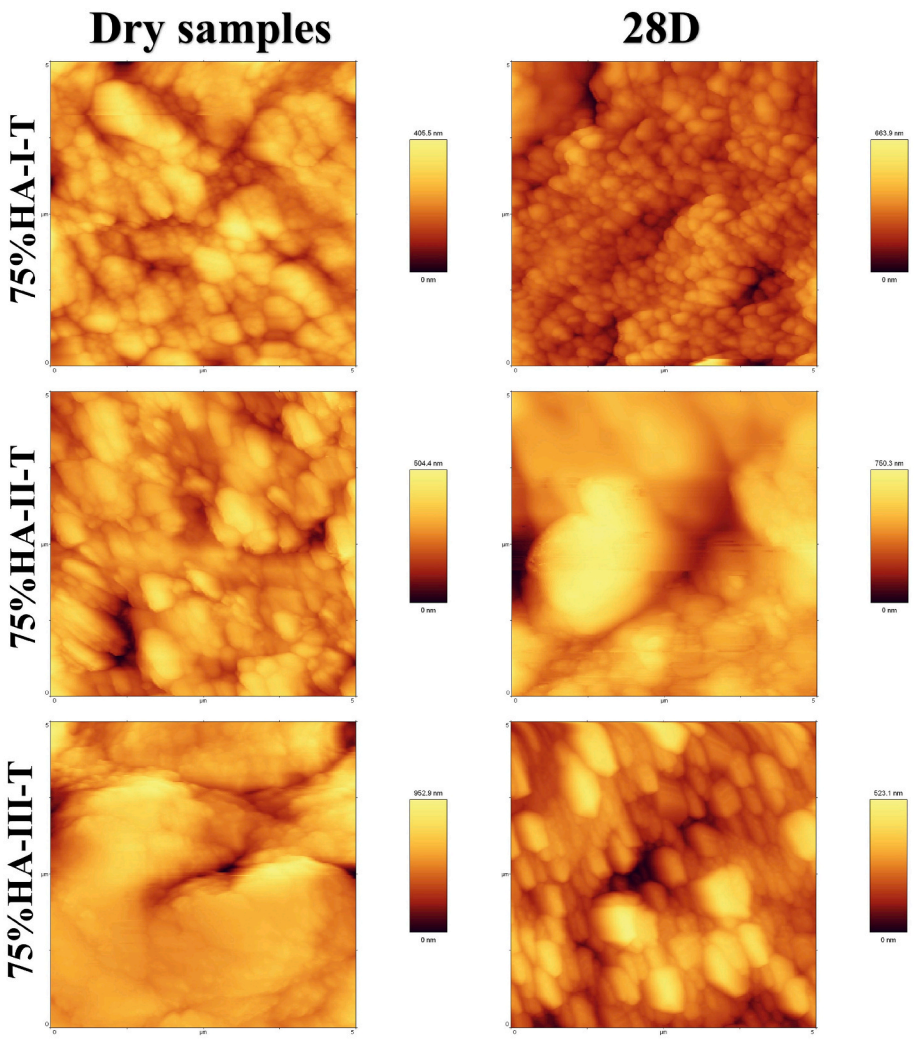

Fig. 15. AFM analysis of the composites before and after immersion in SBF for 28 days in topographical mode.

Table 8
Samples roghness values obtained from AFM analysis.

Sample	Before exposure to SBF	After 28 days of exposure to SBF
75 %HA-I-T	R_a = 118.06 nm	R_a = 88.91 nm
75 %HA-II-T	R_a = 105.81 nm	R_a = 81.25 nm
75 %HA-III-T	R_a = 125.14 nm	R_a = 87.30 nm

that attributed to hydroxyapatite (HA) phase [21]. As mentioned earlier in XRD, the sample surface began to dissolve in the initial days of exposure to the SBF, accompanied by precipitation of new minerals. Over time, new precipitates became more stable [77]. Based on figures by day 28 of exposure to simulated body fluid (SBF), they had fully crystallized and formed final aggregates of new hydroxyapatite on the surface [56]. According to the samples, the 75 %HA-I-T sample has smaller final hydroxyapatite particles than 75 %HA-II-T, which can be attributed to the size of the initial powder synthesis via two different methods. Moreover, the formed precipitates in 75 %HA-III-T showed a plate-like morphology that differs from other's pattern. Thus, relying only on XRD data may not fully capture the samples decomposition and precipitation behavior in SBF. Besides, the EDX analyses of the three composite samples after 28 days of exposure to SBF have been illustrated. Based on EDX data measurements, the calcium-to-phosphorus ratio of the mineralized phase is approximately 1.76. This confirms the presence of precipitates that are enriched in calcium and phosphorus, exhibiting a Ca/P ratio that approaches that of stoichiometric hydroxyapatite [80].

3.4.3. AFM results of SBF-immersed tablets

Fig. 15 shows the surface topography results obtained from AFM analysis. According to the images, the surface of 75 %HA-I-T sample in dry state showed less roughness than its 28-day state after immersion in the SBF solution. This is in agreement with the FESEM results. In other words, these protrusions could be the aggregations of new mineral phase deposited due to the dissolution of the initial composite and the interaction of its resulting ions with the aqueous environment. These changes also occurred in the other two composite samples. In 75 %HA-II-T, the initial protrusions are similar to the previous sample. However, the 28 days of immersion resulted in some differences when compared to the 75 %HA-I-T-28D. Also, the 75 %HA-III-T has fewer elevations than the previous two. After 28 days of exposure to SBF, it shows a different morphology, similar to the results obtained from FESEM. This is related to the production method of this type of composite, which is done by physically mixing the glass and ceramic powders and applying the SPS process. Among the three samples, the 75 %HA-I-T demonstrates a more active surface both before and after contact with SBF. An active dry surface increases the likelihood of mineral phase formation, as shown by snapshots after 28 days of immersion. Besides, Table 8 reported the average roughness values (R_a) of the samples before and after SBF immersion. The results support the mechanism of surface mineralization that occurs after exposure to simulated body fluid (SBF). However, these

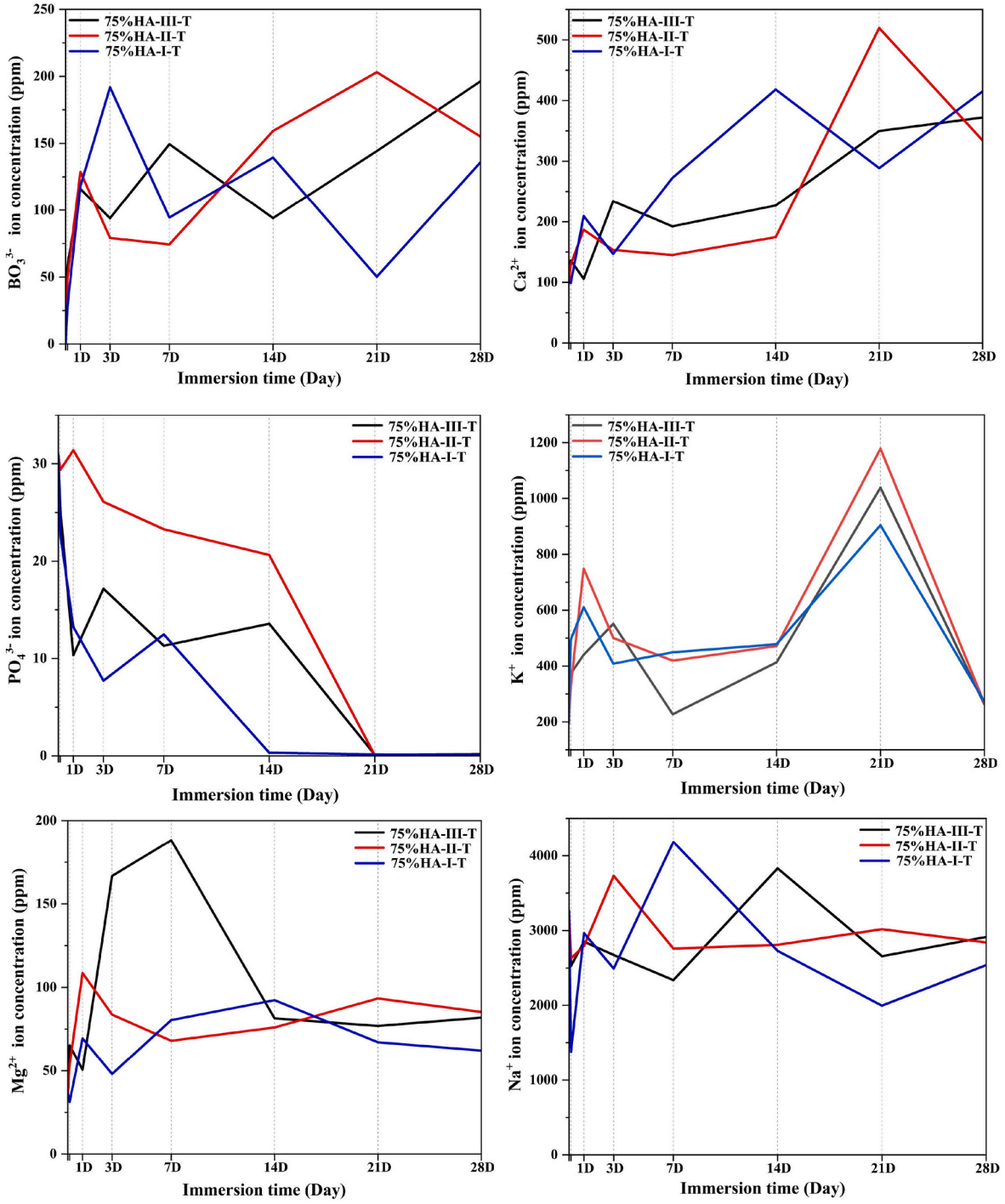

Fig. 16. ICP-OES analysis results of composite tablets in SBF.

values somehow decrease or slowly changes by forming a mineral layer on the sample surface. The gradual degradation of calcium and phosphate from the surface has resulted in a slight reduction in surface roughness, indicating increased regularity and the formation of a bone layer [81,82].

3.4.4. *ICP-OES results of SBF-immersed tablets*

Fig. 16 shows the ion concentration resulting from the tablet's dissolution in the SBF. The results represent borate ion (BO_3^{3-}) release from three composites in SBF. The 75 %HA-I-T sample continuously released borate ions, while the 75 %HA-II-T and 75 %HA-III-T samples initially absorbed them. By day 14, the behavior of the 75 %HA-I-T matched that of the 75 %HA-II-T. As a result, borate concentration increased until day 14 and then stabilized, while the 75 %HA-III-T sample continued the absorption for 28 days [13,14,83]. Besides, the initial Ca^{2+} concentration in SBF was 100 ppm. After immersion, 75 % HA-I-T and 75 %HA-II-T formed a calcium phosphate layer within 1–3 days, while 75 %HA-III-T exhibited the same pattern by day 7, followed by calcium release by day 14. Furthermore, the 75 %HA-I-T had slower calcium release from 14 to 28 days, and 75 %HA-II-T showed higher adsorption due to a more active surface [62,83,84]. Moreover, the initial PO_4^{3-} concentration in the SBF solution is about 31 ppm, leading to calcium phosphate precipitation on sample surfaces, as shown by FESEM results. The PO_4^{3-} concentration remains stable over 28 days, indicating

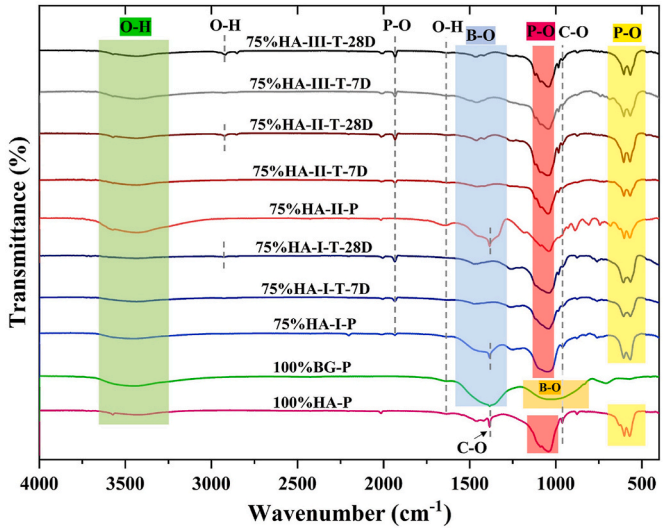

Fig. 17. FTIR results of dry and SBF contained samples in comparison to pure HA and BG.

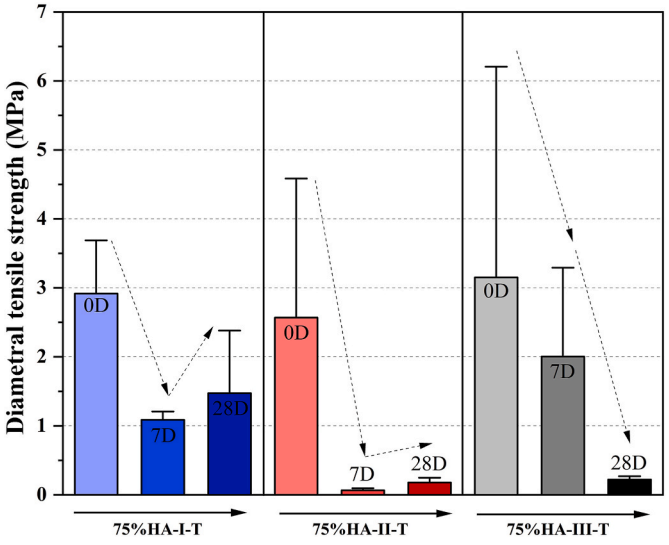

Fig. 18. Results of diametral tensile strength tests of composite tablets after immersion in SBF.

an adsorption process. Phosphate ions, essential for hydroxyapatite formation, are present in both the SBF and the samples. Eventually, these samples release and then adsorb calcium through phosphate ions, resulting in complete PO_4^{3-} adsorption [62,83]. In the following, the initial concentration of K^+ ions in the SBF solution is about 195 ppm. On the first day, all three samples adsorbed K^+. From days 1–14, the 75 % HA-II-T and 75 %HA-I-T samples exhibited both adsorption and release of K^+, with a greater release in the 75 %HA-II-T sample. The 75 % HA-III-T sample only released K^+ ions initially, with no adsorption from days 7–14. Between days 14 and 28, all samples showed both adsorption and release of potassium ions. In addition, the initial concentration of Mg^{2+} ions in SBF is about 36 ppm. Both 75 % HA-III-T and 75 %HA-II-T samples initially release Mg^{2+} ions, with 75 %HA-II-T exhibiting a stronger trend. After three days, both samples begin to absorb Mg^{2+} ions. Between days 3 and 28, they alternate between releasing and reabsorbing Mg^{2+}, with 75 %HA-III-T showing significant release in the first 7 days, followed by increased absorption. Throughout the duration, the changes observed in 75 %HA-I-T were relatively minor compared to others. Finally, the initial Na^+ concentration in SBF is about 3264 ppm. The 75 %HA-I-T adsorbs Na^+ on the first day, while 75 %HA-II-T releases it significantly. The 75 %HA-III-T both adsorbs and releases Na^+ over the same period, with similar trends across all samples from days 3–28. In conclusion, borate glass is recognized for containing various ions in addition to phosphate and calcium ions. These ions have been studied due to the significant tendency of borate glass to dissipate. XRD analysis shows that when immersed in simulated body fluid (SBF), additional phases can appear alongside the intended phase. Furthermore, changes in the concentration of these ions are linked to this phenomenon [13,14,62,83].

3.4.5. FTIR results

The results of the FTIR spectrum are shown in Fig. 17. According to the figure, the range of 500–700 cm^{-1}, which has two different bands, represents the bending vibrations of the PO_4^{3-} groups. These vibrations are known as ν_4. These vibrations arise due to the change in the P-O-P bond angle in the containing plane. Also, in the range of 800–1200 cm^{-1}, an intense band of stretching and asymmetric vibrations of the P-O bond can be observed. In other words, one of the P-O bonds in the phosphate group is stretched, while the other three similar complexes will be closer together. As can be seen from the curves, both of the synthesized composite powders have these bands, which is proof of the high hydroxyapatite content in the initial structure of these composites. In addition, the presence of the bands above and a P-O band in the 1830 cm^{-1} range only in 28 days immersion-composites also indicates the formation of bone tissue in the competition between dissolution and mineralization of these samples in SBF [26,85–88]. Two bands at 960 $cm^{-1}$and 1384 cm^{-1} are also visible. These two bands belong to the C-O groups in CO_3^{2-}. According to Ref. [26], it is claimed to be evidence of the initial formation of an amorphous hydroxyapatite layer that will be converted to pure hydroxyapatite upon further mineralization. Also, glass powder has been examined to prove the presence of boron-based bioactive glass in composites. The leading bands related to the B-O bond are presented below. In the range of 600–800 cm^{-1}, the bending vibrations of B-O-B in the BO_3 and BO_4 groups can be observed. Also, in the range of 800–1200 cm^{-1}, the stretching vibrations of the B-O bond in the tetragonal BO_4 groups are observed as a broadband. Furthermore, B-O stretching vibrations in the trigonal BO_3 group are also indicated in blue in the range of 1200–1600 cm^{-1} [13,14]. As is evident from the spectrum, the bands of B-O have gradually disappeared with the increase in the SBF-immersion time. This is strongly consistent with the results of ICP, which indicate the release of borate boron in the environment. Also, the initial claim of this study that boron affects improving the mineralization process can be proven by these spectra. Finally, O-H groups from water absorption are also visible at 1630 cm^{-1}, 2850 cm^{-1}, and 3400 cm^{-1}, which have higher intensity in glass structures due to their high water absorption [26,89–91]. In this research, the presence of the same background between 100 %HA-P and 75 %HA-I-T can declare the role of HA and BG via method I. Hydroxyapatite was a solution and covered the BG particles. The trend in 75 % HA-I-T is also in agreement with the mentioned criteria. After 7 and 28 days of immersion in SBF, the intensity of the HA characteristic bands have been improved. These proved the effectiveness of in-vitro analysis for this sample. Moreover, sample 75 %HA-II-T is also shown. Unike the 75 %HA-I-T, the glassy background with broad bands justified the matrix role of BG solution in method II. The increment in immersion time caused an intensification in the characteristic bands of HA. These bands are a sign of mineralization after the in-vitro test. In addition to these samples, the physical mixing one called 75 %HA-III-T has been incubated in SBF for 7 and 28 days. The HA characteristic bands have high strength in the sample after 28 days which could show the mineralization happens greatly in the mentioned sample as well.

3.4.6. Mechanical test results of SBF-immersed tablets

The diametral tensile strength (DTS) test results for the composite samples before and after exposure to simulated body fluid (SBF) are

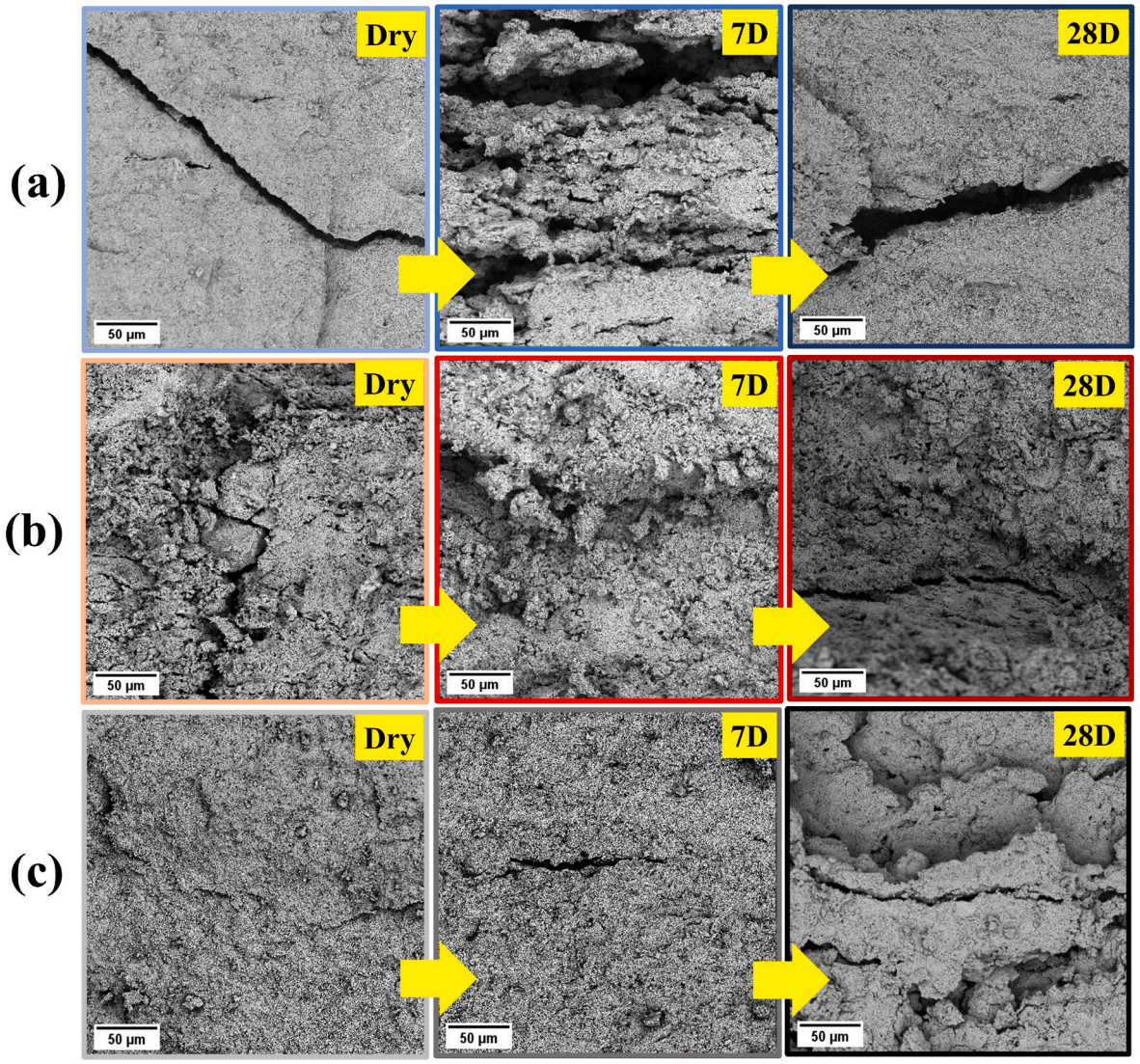

Fig. 19. FESEM images of the fracture surface of biomaterials after DTS testing, a) 75 %HA-I-T, b) 75 %HA-II-T, and c) 75 %HA-III-T.

illustrated in Fig. 18. The 75 %HA-I-T sample has a tensile strength of 2.9 ± 1.1 MPa, comparable to cancellous bone's mechanical strength equal to 7.6 MPa [92]. Moreover, the mechanical behavior of samples was investigated after different time of SBF exposure. After 7 days of immersion, the strength of 75 %HA-I-T sample decreased to 1.1 ± 0.2 MPa, which could imply sample decomposition and ion release. The sample showed reduced mechanical strength due to solution penetration. However, 75 %HA-I-T sample maintained tensile stability, suggesting preserved mechanical properties [93]. Furthermore, the 75 % HA-II-T exhibits a strength of 2.6 ± 2.9 MPa in a dry state, consistent with the 75 %HA-I-T and similar to bone strength. However, its strength significantly decreased after 7 and 28 days immersion in simulated body fluid (SBF), contrasting with previous sample results. This discrepancy may be attributed to the coarser particle size of the initial powder, causing disruptions in internal compression during spark plasma sintering (SPS). Also, the hydroxyapatite phase used as the nucleator in method II possesses greater strength than BG due to its ceramic nature, indicating that a higher pressure may be required for pressing these particles compared to the 75 %HA-I-T [94]. Besides, the 75 %HA-III-T sample exhibits a dry strength of 3.2 ± 4.3 MPa and showed a higher range of variation than the other samples, indicating heterogeneity confirmed by previous analyses. After being immersed in SBF for 7 and 28 days, the sample's strength decreased with increased immersion time. Hence, higher phase homogeneity in other two methods caused an improvement in mechanical properties and maintetance over immersion time [74]. Finally, the 75 %HA-I-T sample exhibits superior mechanical properties due to the retaining of its strength even after immersing in simulated body fluid (SBF).

3.4.7. FESEM results of SBF-immersed tablets after mechanical test

FESEM analysis of the fracture surface of composites after immersion in SBF is shown in Fig. 19. According to these images, all three samples have high structural integrity in the dry state. After 7 days of SBF immersion, cracks of different sizes have formed inside the samples. The mentioned microcracks could result from the structural weakness and inhomogenities produced during synthesis or manufacturing method and or during mechanical investigations [95]. Based on figures related to 28 days of immersion, the discontinuous microcracked structures were intensified. Based on Fig. 19(a), (b) and (c), the 75 %HA-I-T sample shows better mechanical properties and stability than the other two samples after 7 and 28 days. Although it lost some strength due to solution penetration, it still outperforms the others that is clearly illustrated in Fig. 19(a).

4. Conclusion

In the present study, in situ 13–93B3 Borate glass (BG)/hydroxyapatite (HA) composite powders were produced using two solution combustion synthesis methods with different weight ratios and mixing orders. The Method I used initially involved mixing solutions of HA with pre-prepared BG particles, while the second approach (Method II) started with initial solutions of BG combined with pre-prepared HA particles. The final mixtures were then prepared for solution combustion synthesis (SCS). In this regard, XRD results clearly showed the presence of the synthesized HA phase alongside the amorphous nature of the glassy phase. The composite tablets were then derived from powders through the spark plasma sintering, considering that the control samples consisted of pre-prepared HA and BG powders. The simulation results demonstrated a peak shift in RDF analysis and a decrease in ionic distance between the phase interfaces, confirming the potential for composition in the control sample. The samples then underwent physical, mechanical, and biological assessments. The XRD analysis identified the optimal samples, which contain 75 % HA phase, characterized by the highest crystallinity index (68 % via Method I) and the lowest amount of unwanted phases (5 % undesirable phase via Method II). The PSA measurements also suggested an average particle size of 32 nm for the optimal sample via method I and 49 nm for method II. The results of FESEM and TEM of the optimized nanoparticles confirmed the presence of nonspherical and irregular shapes of amorphous BG near HA aggregates. The microhardness results of the optimally combined tablets showed that the optimized sample prepared via method I had a hardness of 68 Vickers, which is closer to the hardness of bone among other samples. Additionally, the control sample exhibited a larger range of changes (±105 units), indicating its lower homogeneity compared to the other two samples. Bioactivity was also examined by immersing samples in simulated body fluid (SBF) over time. The characterization results of SBF-immersed samples illustrated the formation of an HA mineral layer on the produced tablets after 28 days. The presence of a P-O band around 1830 cm^{-1} in FTIR results prove the latter criterion. Additionally, the gradual degradation of Ca^{2+} and PO_4^{3-} from the surface (via ICP-OES analysis) has resulted in a slight reduction in surface roughness, as determined by AFM analysis, indicating enhanced regularity and the formation of a bone layer. Additionally, the DTS and FESEM (after fracture) results of the optimal sample obtained via method I showed a slight change from 2.9 ± 1.1 MPa to 1.1 ± 0.2 MPa, indicating the potential to maintain mechanical properties over immersion. The results could indicate the improvement in mechanical properties while preserving biochemical characteristics with changing the synthesis method.

CRediT authorship contribution statement

Neda Sami: Writing – review & editing, Writing – original draft, Visualization, Investigation, Formal analysis. **Sahar Mollazadeh Beidokhti:** Supervision, Methodology, Conceptualization. **Jalil Vahdati Khaki:** Supervision, Methodology, Conceptualization.

Declaration of competing interest

The authors declare that they have no known competing financial interests or personal relationships that could have appeared to influence the work reported in this paper.

Acknowledgement

This research was supported by a financial grant from Ferdowsi University of Mashhad, Iran.

References

[1] D. Bellucci, A. Sola, A. Anesi, R. Salvatori, L. Chiarini, V. Cannillo, Bioactive glass/hydroxyapatite composites: mechanical properties and biological evaluation, Mater. Sci. Eng. C 51 (2015) 196–205.
[2] E. Saiz, A.R. Boccaccini, J. Chevalier, M. Peroglio, Editorial on Bioceramics for Bone Repair, Elsevier, 2018, pp. 821–822.
[3] R. Comesaña, F. Lusquiños, J. Del Val, F. Quintero, A. Riveiro, M. Boutinguiza, J. R. Jones, R.G. Hill, J. Pou, Toward smart implant synthesis: bonding bioceramics of different resorbability to match bone growth rates, Sci. Rep. 5 (2015) 10677.
[4] A.S. Mao, D.J. Mooney, Regenerative medicine: current therapies and future directions, Proc. Natl. Acad. Sci. 112 (2015) 14452–14459.
[5] N.C. Paxton, S.K. Powell, M.A. Woodruff, Biofabrication: the future of regenerative medicine, Tech. Orthop. 31 (2016) 190–203.
[6] L.L. Hench, Bioceramics: from concept to clinic, J. Am. Ceram. Soc. 74 (1991) 1487–1510.
[7] G. Bolelli, D. Bellucci, V. Cannillo, L. Lusvarghi, A. Sola, N. Stiegler, P. Müller, A. Killinger, R. Gadow, L. Altomare, Suspension thermal spraying of hydroxyapatite: microstructure and in vitro behaviour, Mater. Sci. Eng. C 34 (2014) 287–303.
[8] N. Stiegler, D. Bellucci, G. Bolelli, V. Cannillo, R. Gadow, A. Killinger, L. Lusvarghi, A. Sola, High-velocity suspension flame sprayed (HVSFS) hydroxyapatite coatings for biomedical applications, J. Therm. Spray Technol. 21 (2012) 275–287.
[9] J. Zhao, Y. Liu, W.-b. Sun, H. Zhang, Amorphous calcium phosphate and its application in dentistry, Chem. Cent. J. 5 (2011) 1–7.
[10] M. Vallet-Regí, Ceramics for medical applications, J. Chem. Soc., Dalton Trans. (2001) 97–108.
[11] S.V. Dorozhkin, Calcium orthophosphate bioceramics, Ceram. Int. 41 (2015) 13913–13966.
[12] R.Z. LeGeros, Properties of osteoconductive biomaterials: calcium phosphates, Clin. Orthop. Relat. Res. 395 (2002) 81–98.
[13] M. Ghanad, N. Akrami, P. Keil, H. Bradtmüller, M.R. Hansen, J.V. Khaki, S. M. Beidokhti, Single-step solution combustion synthesis of porous 1393-B3 glass powders and structural characterization via solid-state NMR spectroscopy, Ceram. Int. 49 (2023) 14689–14701.
[14] N. Akrami, M. Ghanad, P. Keil, H. Bradtmüller, M.R. Hansen, S. Kargozar, J. V. Khaki, S.M. Beidokhti, Microstructural properties and in vitro dissolution of microporous bioactive 13-93B3 glass powders synthesized via solution combustion synthesis, J. Non-Cryst. Solids 615 (2023) 122425.
[15] F.H. Nielsen, Is boron nutritionally relevant? Nutr. Rev. 66 (2008) 183–191.
[16] P. Balasubramanian, T. Büttner, V.M. Pacheco, A.R. Boccaccini, Boron-containing bioactive glasses in bone and soft tissue engineering, J. Eur. Ceram. Soc. 38 (2018) 855–869.
[17] R.K. Brow, Reactions of Borate Glasses in Aqueous Solutions, 2022.
[18] A. Gharbi, H. Oudadesse, H. El Feki, W. Cheikhrouhou-Koubaa, X. Chatzistavrou, J. V. Rau, J. Heinämäki, I. Antoniac, N. Ashammakhi, N. Derbel, High boron content enhances bioactive glass biodegradation, J. Funct. Biomater. 14 (2023) 364.
[19] F.N. Oktar, G. Göller, Sintering effects on mechanical properties of glass-reinforced hydroxyapatite composites, Ceram. Int. 28 (2002) 617–621.
[20] G. Goller, H. Demirkıran, F.N. Oktar, E. Demirkesen, Processing and characterization of bioglass reinforced hydroxyapatite composites, Ceram. Int. 29 (2003) 721–724.
[21] D. Angioni, R. Orrù, G. Cao, S. Garroni, D. Bellucci, V. Cannillo, Bioactivity enhancement by a ball milling treatment in novel bioactive glass-hydroxyapatite composites produced by spark plasma sintering, J. Eur. Ceram. Soc. 43 (2023) 1220–1229.
[22] X. Chatzistavrou, K. Chrissafis, E. Kontonasaki, T. Zorba, P. Koidis, K. M. Paraskevopoulos, Sintered hydroxyapatite/bioactive glass composites: thermal Analysis and Bioactivity, Key Eng. Mater. 309 (2006) 167–170.
[23] D. Bellucci, L. Desogus, S. Montinaro, R. Orrù, G. Cao, V. Cannillo, Innovative hydroxyapatite/bioactive glass composites processed by spark plasma sintering for bone tissue repair, J. Eur. Ceram. Soc. 37 (2017) 1723–1733.
[24] Q. Chen, J.L. Xu, L. Yu, X.-Y. Fang, K.A. Khor, Spark plasma sintering of sol–gel derived 45S5 Bioglass®-ceramics: mechanical properties and biocompatibility evaluation, Mater. Sci. Eng. C 32 (2012) 494–502.
[25] A. Bellosi, F. Monteverde, D. Sciti, Fast densification of ultra-high-temperature ceramics by spark plasma sintering, Int. J. Appl. Ceram. Technol. 3 (2006) 32–40.
[26] M. Rizwan, M. Hamdi, W.J. Basirun, K. Kondoh, J. Umeda, Low pressure spark plasma sintered hydroxyapatite and Bioglass® composite scaffolds for bone tissue repair, Ceram. Int. 44 (2018) 23052–23062.
[27] D. Bellucci, A. Sola, V. Cannillo, Low temperature sintering of innovative bioactive glasses, J. Am. Ceram. Soc. 95 (2012) 1313–1319.
[28] A. Motealleh, S. Eqtesadi, F.H. Perera, A.L. Ortiz, P. Miranda, A. Pajares, R. Wendelbo, Reinforcing 13–93 bioglass scaffolds fabricated by robocasting and pressureless spark plasma sintering with graphene oxide, J. Mech. Behav. Biomed. Mater. 97 (2019) 108–116.
[29] Y. Gu, N. Loh, K. Khor, S. Tor, P. Cheang, Spark plasma sintering of hydroxyapatite powders, Biomaterials 23 (2002) 37–43.
[30] M. Speth, K.R. Riedmueller, M. Liewald, Study on Mixing Behaviour of Aluminium-Ceramic Powder Having High SiC Volume Fractions up to 50 vol.%, Functional Composite Materials, vol. 4, 2023, p. 8.
[31] Q. Wang, J. Shi, First-principles analysis of SiC/Al composites interface, Int. J. Fluid Mech. Therm. Sci. 5 (2019) 91.
[32] X. Li, J. Sun, X. Wei, L. Li, H. Jin, L. Guo, Molecular dynamics study with COMPASS II forcefield on nucleation and growth mechanism of sodium chloride in supercritical water, J. Supercrit. Fluids 202 (2023) 106053.

[33] Z. Mollaei, F. Kermani, F. Moosavi, M. Kahani, S. Mollazadeh, J.V. Khaki, Elaboration of entropy with glass composition: a molecular dynamics study, Mater. Today Commun. 33 (2022) 104340.
[34] W. Yang, D. Xu, Y. Diao, J. Zhao, Z. Jing, Y. Guo, Molecular dynamics simulations on K2SO4 nucleation in supercritical water, J. Mol. Liq. 367 (2022) 120565.
[35] T. Hawa, M. Zachariah, Molecular dynamics simulation and continuum modeling of straight-chain aggregate sintering: development of a phenomenological scaling law, Phys. Rev. B Condens. Matter 76 (2007) 054109.
[36] S. Park, J.O. Baker, M.E. Himmel, P.A. Parilla, D.K. Johnson, Cellulose crystallinity index: measurement techniques and their impact on interpreting cellulase performance, Biotechnol. Biofuels 3 (2010) 10.
[37] S. Nam, Y. Liu, Z. He, D.J. Hinchliffe, D. Fang, Assessment of Segal method for identifying crystallinity evolution in developing cotton fibers, Agricultural & Environmental Letters 9 (2024) e20138.
[38] Y. Cheah, K. Masaharu, Comparison of crystallinity index computational methods based on lignocellulose X-ray diffractogram, Materials Research Foundations (2023) 29.
[39] T. Kokubo, H. Takadama, How useful is SBF in predicting in vivo bone bioactivity? Biomaterials 27 (2006) 2907–2915.
[40] J. Swab, G.D. Quinn, Fractographic Analysis of Ceramic Materials Tested Using the Diametral Compression Test, 2017.
[41] A. Procopio, A. Zavaliangos, J. Cunningham, Analysis of the diametrical compression test and the applicability to plastically deforming materials, J. Mater. Sci. 38 (2003) 3629–3639.
[42] J. Horabik, J. Wiącek, P. Parafiniuk, M. Stasiak, M. Bańda, M. Molenda, Tensile strength of pressure-agglomerated potato starch determined via diametral compression test: discrete element method simulations and experiments, Biosyst. Eng. 183 (2019) 95–109.
[43] A.J. Holder, L. Ye, Quantum mechanical quantitative structure–activity relationships to avoid mutagenicity, Dent. Mater. 25 (2009) 20–25.
[44] A.V. Saghir, S.M. Beidokhti, J.V. Khaki, A. Salimi, One-step synthesis of single-phase (Co, Mg, Ni, Cu, Zn) O High entropy oxide nanoparticles through SCS procedure: thermodynamics and experimental evaluation, J. Eur. Ceram. Soc. 41 (2021) 563–579.
[45] T. Xia, T. Liu, W. Zhao, B. Ma, T. Wang, Self-propagating high-temperature synthesis of Al2O3-TiC-Al composites by aluminothermic reactions, J. Mater. Sci. 36 (2001) 5581–5584.
[46] M.T. Islam, L. Macri-Pellizzeri, V. Sottile, I. Ahmed, Rapid conversion of highly porous borate glass microspheres into hydroxyapatite, Biomater. Sci. 9 (2021) 1826–1844.
[47] S. Takayama, Amorphous structures and their formation and stability, J. Mater. Sci. 11 (1976) 164–185.
[48] D.J. Indrani, B. Soegijono, W.A. Adi, N. Trout, Phase composition and crystallinity of hydroxyapatite with various heat treatment temperatures, Int. J. Appl. Pharm. 9 (2017) 87–91.
[49] G. Rh Owen, M. Dard, H. Larjava, Hydoxyapatite/beta-tricalcium phosphate biphasic ceramics as regenerative material for the repair of complex bone defects, J. Biomed. Mater. Res. B Appl. Biomater. 106 (2018) 2493–2512.
[50] K. Aoyagi, R. Sivakumar, X. Yi, T. Watanabe, T. Akiyama, Effect of diluents on high purity β-SiAlONs by mechanically activated combustion synthesis, J. Ceram. Soc. Jpn. 117 (2009) 777–779.
[51] L. Gu, G. Meng, Powder synthesis and characterization of nanocrystalline CeO2 via the combustion processes, Mater. Res. Bull. 42 (2007) 1323–1331.
[52] J.M. Hughes, M. Cameron, K.D. Crowley, Structural variations in natural F, OH, and Cl apatites, Am. Mineral. 74 (1989) 870–876.
[53] B.E. Warren, X-Ray Diffraction, 1990. Courier Corporation.
[54] U. Younas, M. Atif, A. Anjum, M. Nadeem, T. Ali, R. Shaheen, W. Khalid, Z. Ali, Fabrication of La 3+ doped Ba 1− x La x TiO 3 ceramics with improved dielectric and ferroelectric properties using a composite-hydroxide-mediated method, RSC advances 13 (2023) 5293–5306.
[55] G. Sun, D. Fan, S. Tao, Effect of the mass fraction of ceramic particles on the porosity of wear-resistant composites fabricated by combustion synthesis, Metall. Mater. Trans. 49 (2018) 5661–5670.
[56] F. Kermani, S. Mollazadeh Beidokhti, F. Baino, Z. Gholamzadeh-Virany, M. Mozafari, S. Kargozar, Strontium-and cobalt-doped multicomponent mesoporous bioactive glasses (MBGs) for potential use in bone tissue engineering applications, Materials 13 (2020) 1348.
[57] W.D. Callister Jr., D.G. Rethwisch, Materials Science and Engineering: an Introduction, John wiley & sons, 2020.
[58] F. Absalan, M.S. Sadjadi, N. Farhadyar, M.H. Sadr, Synthesis of mesoporous hydroxyapatite with controlled pore size using the chitosan as an organic modifier: investigating the effect of the weight ratio and pH value of chitosan on the structural and morphological properties, J. Inorg. Organomet. Polym. Mater. 30 (2020) 3562–3573.
[59] S. Ebrahimi, Y.U. Hanim, C.S. Sipaut, N.b.A. Jan, S.E. Arshad, S.E. How, Fabrication of hydroxyapatite with bioglass nanocomposite for human wharton's-jelly-derived mesenchymal stem cell growing substrate, Int. J. Mol. Sci. 22 (2021) 9637.
[60] S. Izadi, S. Hesaraki, M. Hafezi-Ardakani, Evaluation nanostructure properties of bioactive glass scaffolds for bone tissue engineering, Adv. Mater. Res. 829 (2014) 289–293.
[61] H. Aali, S. Mollazadeh, J.V. Khaki, Quantitative evaluation of ambient O2 interference during solution combustion synthesis process: considering iron nitrate–fuel system, Ceram. Int. 45 (2019) 17775–17783.
[62] F.D. Haghighi, S.M. Beidokhti, Z.T. Najaran, S.S. Saghi, Highly improved biological and mechanical features of bioglass-ceramic/gelatin composite scaffolds using a novel silica coverage, Ceram. Int. 47 (2021) 14048–14061.
[63] F. Kermani, A. Gharavian, S. Mollazadeh, S. Kargozar, A. Youssefi, J.V. Khaki, Silicon-doped calcium phosphates; the critical effect of synthesis routes on the biological performance, Mater. Sci. Eng. C 111 (2020) 110828.
[64] Molecular dynamics study of complex dopant electrolyte Nd2–xHoxZr2O7: structure, conductivity, and thermal expansion, Fuel Cells 13 (2013) 1048–1055.
[65] I. Fairushin, S. Khrapak, A. Mokshin, Direct evaluation of the physical characteristics of Yukawa fluids based on a simple approximation for the radial distribution function, Results Phys. 19 (2020) 103359.
[66] D. Zang, J. Becker, U. Betke, G. Hasemann, K. Khanchych, B. Gorr, M. Krüger, Phase evolution during high-energy ball milling and annealing of Ti-doped Mo-V-Si-B alloys, Materials 18 (2025) 2494.
[67] M. Saghir, M.A. Umer, A. Ahmed, N. Bint Monir, U. Manzoor, A. Razzaq, L. Xian, K. Mohammad, M. Shahid, Y.-K. Park, Effect of high energy ball milling and low temperature densification of plate-like alumina powder, Powder Technol. 383 (2021) 84–92.
[68] C.A. Rizwan M, M. Sohail, N.M. Bashir, S. Yousuf, R. Alias, M. Hamdi, J.W. Basirun, Bioglass-fibre reinforced hydroxyapatite composites synthesized using spark plasma sintering for bone tissue engineering, Process. Appl. Ceram. 15 (2021) 270–278.
[69] M. Rizwan, K. Genasan, M.R. Murali, H.R.B. Raghavendran, R. Alias, Y.Y. Cheok, W.F. Wong, A. Mansor, M. Hamdi, W.J. Basirun, In vitro evaluation of novel low-pressure spark plasma sintered HA–BG composite scaffolds for bone tissue engineering, RSC advances 10 (2020) 23813–23828.
[70] D. Bellucci, A. Sola, L. Lusvarghi, V. Cannillo, Hydroxyapatite–tricalcium phosphate–bioactive glass ternary composites, Ceram. Int. 40 (2014) 3805–3808.
[71] E. Lantsev, N. Malekhonova, V. Chuvildeev, A. Nokhrin, M. Boldin, P. Andreev, K. Smetanina, Effect of initial particle size and various composition on the spark plasma sintering of binderless tungsten carbide. Journal of Physics: Conference Series, IOP Publishing, 2021 012022.
[72] A. Heydarian, S. Abdolkarim Sajjadi, M. Johnsson, A proposed model for spark plasma sintering of SiC-Si nanocomposite with different SiC particle sizes, J. Compos. Mater. 54 (2020) 2599–2609.
[73] B. Sadeghi, P. Cavaliere, M. Sanayei, Effect of reinforcement particle size on the corrosion and mechanical properties of spark plasma sintered aluminium matrix composites, J. Microsc. 297 (2025) 18–34.
[74] O. Parkhomei, N. Pinchuk, O. Sych, T. Tomila, G. Tovstonog, V. Gorban', Y. I. Yevych, O. Kuda, Structural and mechanical properties of bioactive glass–ceramic composites, Powder Metall. Met Ceram. 55 (2016) 172–184.
[75] S. Stea, M. Visentin, L. Savarino, G. Ciapetti, M. Donati, A. Moroni, V. Caja, A. Pizzoferrato, Microhardness of bone at the interface with ceramic-coated metal implants, J. Biomed. Mater. Res. 29 (1995) 695–699.
[76] M. Trzaskowska, V. Vivcharenko, A. Przekora, The impact of hydroxyapatite sintering temperature on its microstructural, mechanical, and biological properties, Int. J. Mol. Sci. 24 (2023) 5083.
[77] L.-G. Yu, K. Khor, H. Li, P. Cheang, Effect of spark plasma sintering on the microstructure and in vitro behavior of plasma sprayed HA coatings, Biomaterials 24 (2003) 2695–2705.
[78] S.V. Dorozhkin, Calcium orthophosphates as bioceramics: state of the art, J. Funct. Biomater. 1 (2010) 22–107.
[79] L. Fu, H. Engqvist, W. Xia, Glass–ceramics in dentistry: a review, Materials 13 (2020) 1049.
[80] S. Ramesh, C. Tan, M. Hamdi, I. Sopyan, W. Teng, The influence of Ca/P ratio on the properties of hydroxyapatite bioceramics. International Conference on Smart Materials and Nanotechnology in Engineering, 2007, pp. 855–860. SPIE.
[81] F.D. Haghighi, N. Sami, M. Azizi, S.M. Beidokhti, A.R. Kiani Rashid, Sol-gel-synthesized bioglass-ceramics: physical, mechanical, and biological properties, Journal of the Australian Ceramic Society (2024) 1–17.
[82] I. Leonor, A. Ito, K. Onuma, N. Kanzaki, Z. Zhong, D. Greenspan, R. Reis, In situ study of partially crystallized Bioglass® and hydroxylapatite in vitro bioactivity using atomic force microscopy, J. Biomed. Mater. Res.: An Official Journal of The Society for Biomaterials, The Japanese Society for Biomaterials, and The Australian Society for Biomaterials and the Korean Society for Biomaterials 62 (2002) 82–88.
[83] X. Liu, M.N. Rahaman, D.E. Day, Conversion of melt-derived microfibrous borate (13-93B3) and silicate (45S5) bioactive glass in a simulated body fluid, J. Mater. Sci. Mater. Med. 24 (2013) 583–595.
[84] J. Zhou, H. Wang, S. Zhao, N. Zhou, L. Li, W. Huang, D. Wang, C. Zhang, In vivo and in vitro studies of borate based glass micro-fibers for dermal repairing, Mater. Sci. Eng. C 60 (2016) 437–445.
[85] Y. Ahmed, S. El-Sheikh, Z. Zaki, Changes in hydroxyapatite powder properties via heat treatment, Bull. Mater. Sci. 38 (2015) 1807–1819.
[86] G. Sauer, W. Zunic, J. Durig, R. Wuthier, Fourier transform Raman spectroscopy of synthetic and biological calcium phosphates, Calcif. Tissue Int. 54 (1994) 414–420.
[87] M. Nara, H. Morii, M. Tanokura, Coordination to divalent cations by calcium-binding proteins studied by FTIR spectroscopy, Biochimica et Biophysica Acta (BBA)-Biomembranes 1828 (2013) 2319–2327.
[88] L. Zhang, Y. Liu, Y. Wang, X. Li, Y. Wang, Investigation of phosphate removal mechanisms by a lanthanum hydroxide adsorbent using p-XRD, FTIR and XPS, Appl. Surf. Sci. 557 (2021) 149838.
[89] H. Gheisari, E. Karamian, M. Abdellahi, A novel hydroxyapatite–Hardystonite nanocomposite ceramic, Ceram. Int. 41 (2015) 5967–5975.
[90] L. Berzina-Cimdina, N. Borodajenko, Research of calcium phosphates using Fourier transform infrared spectroscopy, Infrared spectroscopy-materials science, engineering and technology 12 (2012) 251–263.

[91] M.H. Nawaz, A. Aizaz, A.Q. Ropari, H. Shafique, O.b. Imran, B.Z. Minhas, J. Manzur, M.S. Alqahtani, M. Abbas, M.A. Ur Rehman, A study on the effect of bioactive glass and hydroxyapatite-loaded Xanthan dialdehyde-based composite coatings for potential orthopedic applications, Sci. Rep. 13 (2023) 17842.
[92] S.J. Kaplan, W.C. Hayes, J.L. Stone, G.S. Beaupré, Tensile strength of bovine trabecular bone, J. Biomech. 18 (1985) 723–727.
[93] J. Park, G. Kenner, Effect of electrical stimulation on the interfacial tensile strength and amount of bone formation, Biomaterials, medical devices, and artificial organs 4 (1976) 225–233.
[94] A.M. Deliormanlı, M.N. Rahaman, Direct-write assembly of silicate and borate bioactive glass scaffolds for bone repair, J. Eur. Ceram. Soc. 32 (2012) 3637–3646.
[95] E. Medvedovski, Influence of corrosion and mechanical loads on advanced ceramic components, Ceram. Int. 39 (2013) 2723–2741.